

**Effects of Charge Carrier Transport on Device
Performance of Organic Crystalline Solar Cells**

Mitsuru Kikuchi

SOKENDAI (The Graduate University for Advanced Studies)

School of Physical Sciences

Dept. of Functional Molecular Science

Contents

Chapter 1: General Introduction	1
1.1. Organic Semiconductors	1
1.2. Donor/Acceptor Sensitization	2
1.3. Carrier Transport	5
1.3.1. Band-like Transport in Organic Single Crystals	5
1.3.2. Carrier Range	7
1.4. Impurity Doping in Organic Semiconductors	9
1.4.1. Dopants	9
1.4.2. Mechanism of Impurity Doping	12
1.5. Hall Effect Measurements for Doped Organic Single Crystals	14
1.6. Motivation for This Doctoral Thesis	16
1.7. Thesis Overviews	18
1.8. References	21
Chapter 2: Experimental Equipment and Methods	26
2.1. Purification of Organic Semiconductors	26
2.2. Fabrication of Organic Single Crystals for devices	28
2.3. Experimental Environment	29
2.4. Extremely Low Concentration Doping for Organic Semiconductors	30
2.5. Fabrication of devices	32
2.5.1. Single Crystal Photovoltaic cells	32
2.5.2. Lateral Alternating Multilayered Junction for Organic Solar Cells	33
2.6. Measurements of Photovoltaic Properties	35

2.6.1. General	36
2.6.2. Current Density-Voltage (<i>J-V</i>) Characteristics	37
2.6.3. Action Spectrum	38
2.7. Hall effect Measurement	39
2.8. References	41
Chapter 3: Single Crystal Organic Photovoltaic Cells Using Lateral Electron Transport	42
3.1. Introduction	43
3.2. Experimental	46
3.3. Results and Discussion	48
3.4. Conclusion	53
3.5. References	54
Chapter 4: Lateral Alternating Donor/Acceptor Multilayered Junction for Organic Solar Cells	55
4.1. Introduction	56
4.2. Experimental	61
4.3. Results and Discussion	63
4.3.1. Carrier ranges	63
4.3.2. Lateral Alternating Multilayered Junction	67
4.4. Conclusion	72
4.5. References	73

Chapter 5: Doped Organic Single-Crystal Photovoltaic Cells	76
5.1. Introduction	77
5.2. Experimental	80
5.3. Results and Discussion	82
5.3.1. Characteristics of <i>p</i> -type homoepitaxial layer	82
5.3.2. Doped organic single-crystal photovoltaic cells	84
5.3.3. Calculation for the exciton collection efficiency and exciton diffusion length	87
5.4. Conclusion	91
5.5. References	92
Chapter 6: Thesis Summary	95
List of Publication	96
Acknowledgement	102

Chapter 1: General Introduction

1.1. Organic Semiconductors

In 1954, H. Akamatsu and H. Inokuchi successfully measured the conductivity (σ) of the perylene–bromine complex for the first time.¹⁾ In the 1980s, Tang et al. reported an organic light-emitting diode (OLED)²⁾ and organic photovoltaic (OPV) cell.³⁾ Over the period of approximately 30 years after their study, many device applications have been studied. Organic semiconductor devices have various advantages for commercialization including a low cost, flexibility, small weight, and printability. Utilizing these advantages, Sony Corporation demonstrated the first example of a flexible display using OLEDs in 2007. Subsequently, many televisions and mobile phones using OLEDs have been commercialized (Fig. 1.1). On the other hand, OPVs are not yet widespread even though a power conversion efficiency over 14% has been reported in recent years.^{4,5)} Recently, organic single-crystals with band transport have been discovered.^{6–10)} They are promising to provide novel types of organic devices in our daily life. Impurity doping is a standard technique to control the carrier concentration (N).^{11,12)} Therefore, in this thesis, a fundamental study on OPVs is performed using organic single-crystals and impurity doping techniques and a new type of organic solar cells is developed.

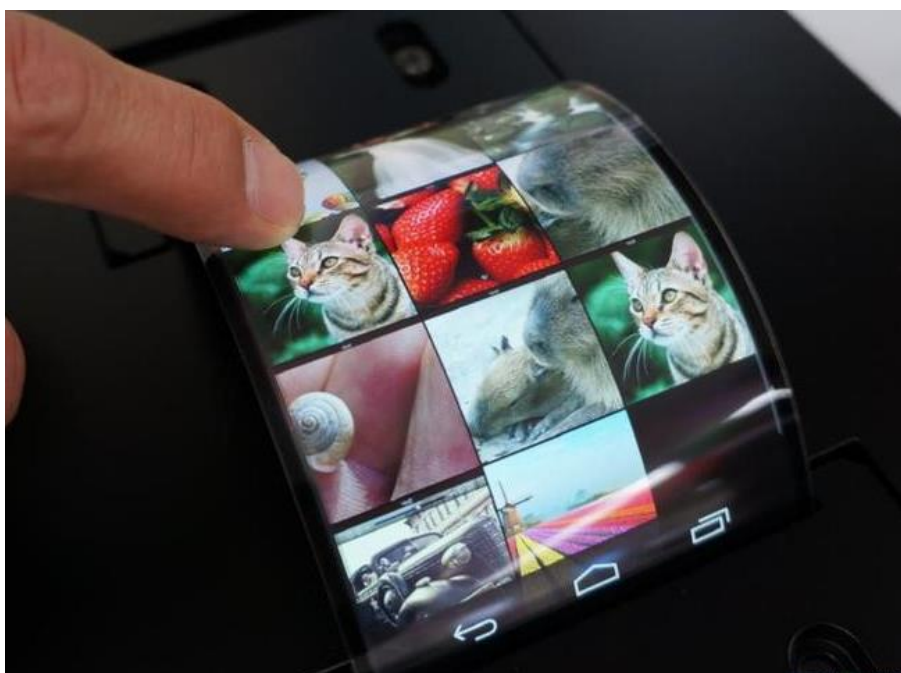


Fig. 1.1 Photograph of a flexible display using OLEDs for mobile phones.

1.2. Donor/Acceptor Sensitization

Organic solar cells (OSCs) have been substantially developed in the last decade. Donor (D)/acceptor (A) sensitization has been crucial in the development. Excitons generated by the absorption of light dissociate into free electrons and holes, which then move to the electrodes by carrier transport; this process is fundamental in the generation of photocurrent. An efficient dissociation of excitons is required for generation of a large photocurrent. However, it is difficult to dissociate excitons in a single organic semiconductor due to the strong attractive forces. The force acting on the positive and negative charges of the exciton (F) is represented by the Coulomb's law:

$$F = \frac{1}{4\pi\epsilon\epsilon_0} \frac{q_1q_2}{r^2} \quad (1.1)$$

where ϵ , ϵ_0 , r , and q are the relative dielectric constant, dielectric constant in vacuum, distance between the charges, and magnitude of each charge, respectively. Inorganic

semiconductors have relatively large $\epsilon (> 10)$, where weakly bound Wannier excitons are formed, which can easily separate into free carriers (Fig. 1.2 (left)). On the other hand, organic semiconductors have relatively small $\epsilon (\sim 4)$, where strongly bound Frenkel excitons are formed, which cannot separate into free carriers (Fig. 1.2 (right)). In order to overcome this problem, a device structure in which two organic semiconductor materials are in contact is required for OSCs. Electrons excited by light irradiation of a single-molecule film relax before dissociation (Fig. 1.3(a)). On the other hand, a combination of a donor molecule (D) and acceptor molecule (A) can separate the positive and negative charges to the highest occupied molecular orbital (HOMO) of D and lowest unoccupied molecular orbital (LUMO) of A, respectively (Fig. 1.3(b)). The separated charges form a charge-transfer (CT) exciton, which can easily dissociate. Therefore, this D/A system is essential in order to obtain a large photocurrent.

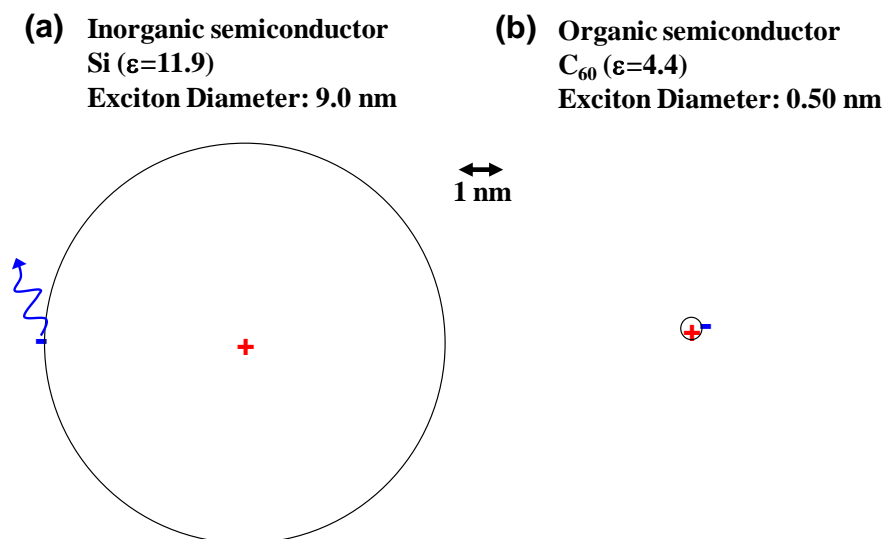


Fig. 1.2 Schematics of a (a) Wannier exciton generated in Si and (b) Frenkel exciton generated in C₆₀.

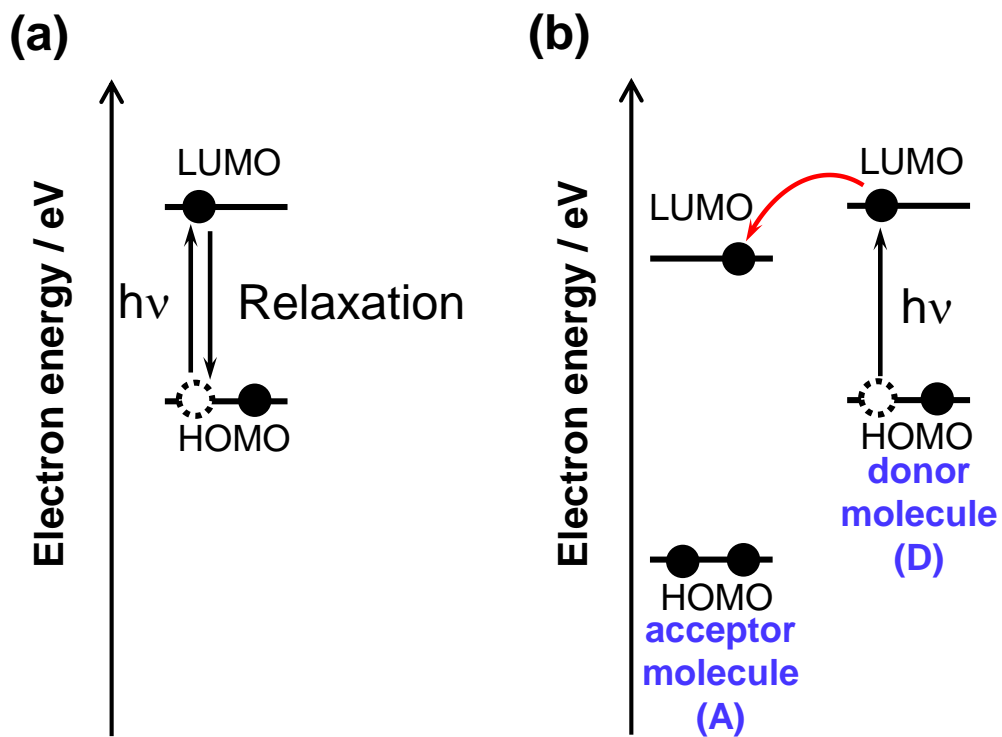


Fig. 1.3 Schematic energy diagrams and models of photo-generated excitons in a (a) single organic semiconductor and (b) D/A system.

1.3. Carrier Transport

1.3.1 Band-like Transport in Organic Single-Crystals

Hopping and band conduction models are important to describe the carrier transport mechanisms in organic semiconductors. The carrier transport in an amorphous film prepared by vapor deposition is explained by hopping conduction based on the Marcus theory.¹⁴⁾

Organic single-crystals have been studied since the 1950's. As organic single-crystals are less influenced by traps due to structural defects than amorphous films, they exhibit remarkably high mobilities. However, in many organic semiconductors, the hopping conduction is still dominant in the carrier transport at room temperature even in materials with crystalline structures.¹⁵⁻¹⁷⁾ These reports suggest that the band conduction is eliminated by phonon scattering due to the considerably narrower bandwidth than that of the inorganic Si. Recently, some organic semiconductors with potential band conduction were reported.¹⁸⁻²³⁾ Fig. 1.4 summarizes the organic semiconductors exhibiting band-like transport. These materials exhibit very high mobilities exceeding $10 \text{ cm}^2\text{V}^{-1}\text{s}^{-1}$. Generally, the band conduction is utilized in analyses of the temperature dependence of the carrier mobility (μ) and Hall effect measurement. The carrier mobility (μ) for band transport can be expressed by:

$$\mu = \frac{e\tau_c}{m^*} \quad (1.2)$$

$$\frac{1}{\tau_c} = \frac{1}{\tau_L} + \frac{1}{\tau_I} \quad (1.3)$$

where τ_c is the mean free time, e is the elementary charge, m^* is the effective mass, and τ_L and τ_I are the mean free times for lattice scattering and impurity scattering, respectively. With the increase in temperature, the lattice scattering increases and μ decreases. τ_L is proportional to the temperature to the power of minus three halves ($\tau_L \propto T^{-3/2}$). On the other hand, with the decrease in temperature, the impurity scattering increases and μ decreases. τ_I is proportional to the temperature to the power of three halves ($\tau_I \propto T^{3/2}$).

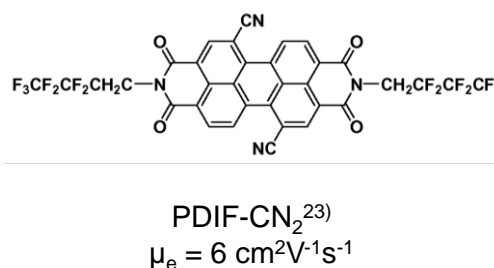
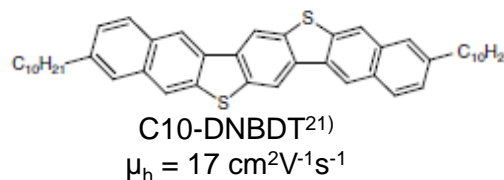
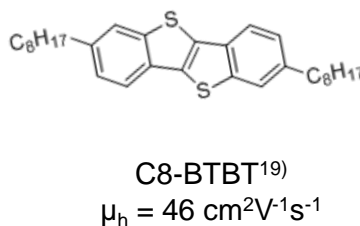
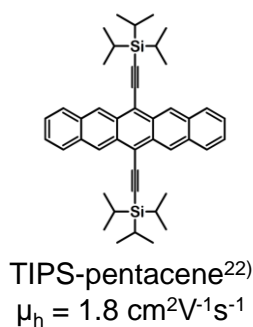
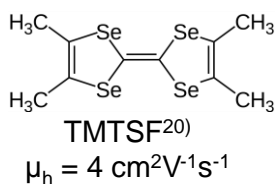
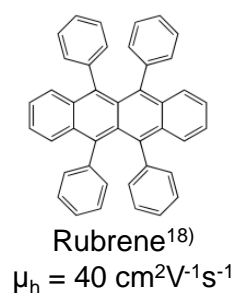


Fig. 1.4 Organic semiconductors exhibiting band-like transport and reported values of carrier mobility at room temperature.

1.3.2 Carrier Range

The carrier transport can be represented by the multiple trap and release (MTR) model.²⁴⁻²⁶⁾ In recent years, it has been reported that this transport model can be applied not only for amorphous films but also for rubrene single-crystals.^{27,28)} A schematic of this model is shown in Fig. 1.5. Shallow and deep traps exist in organic semiconductor films. When holes are captured by the deep traps, they cannot escape using the thermal energy available at room temperature. Therefore, the average time for hole capture by the deep traps corresponds to the deep trapping lifetime (τ_h). On the other hand, when the holes are captured by the shallow traps, they can escape using the thermal energy available at room temperature. Considering the time required for the capture and thermal release processes, the shallow traps dominate in the hole drift mobility (μ_h). The range of the holes (L_h), which is the average distance traveled by the carriers until capture by the deep traps, can be expressed by:

$$L_h = \mu_h \tau_h E \quad (1.4)$$

where μ_h , τ_h , and E are the hole drift mobility, deep trapping lifetime of the holes, and electric field, respectively.

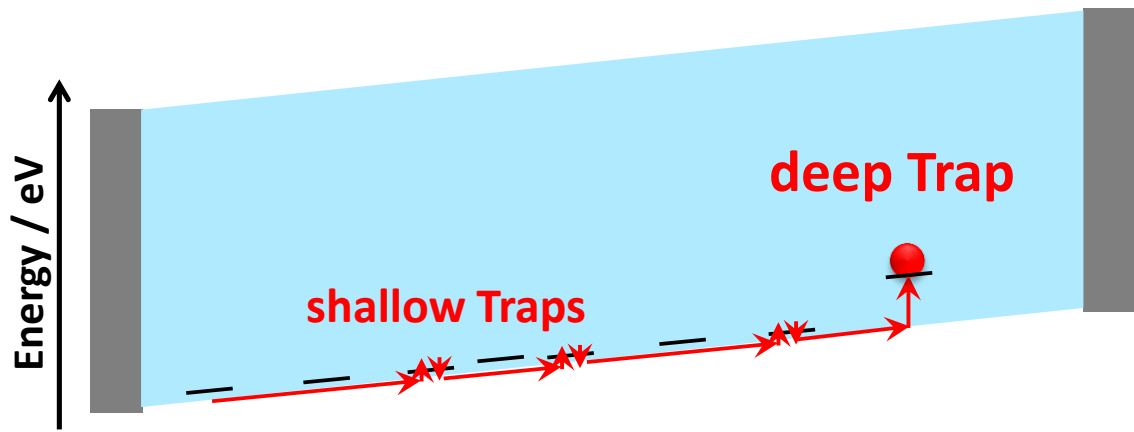


Fig. 1.5 Schematic of the MTR model.

1.4. Impurity Doping in an Organic Semiconductor

1.4.1 Dopants

Fig. 1.6 summarizes the various donor and acceptor dopants for organic semiconductors. In early studies, the *p*-type doping for organic semiconductors using halogen gases such as bromine and iodine^{29,30)} was reported. However, these small gas molecules easily diffuse in organic semiconductors, hindering the precise control of the doping by halogen gases. Therefore, inorganic molecules such as molybdenum oxide (MoO_3),^{31–34)} vanadium oxide (V_2O_5),³⁵⁾ and iron (III) chloride (Fe_2Cl_6),³⁶⁾ which have been used as hole-injection layers for OLEDs, are typically used as acceptor dopants. These dopants can easily withdraw an electron from the organic semiconductor due to its large work function (< 5.5 eV).

On the other hand, Maitrot et al. reported a significant increase in conductivity by a *p*-type doping with organic molecules of 2,3-dichloro-5,6-dicyano-1,4-benzoquinone (DDQ) and tetracyanoquinodimethane (TCNQ).³⁷⁾ Recently, K. Leo's group have carried out systematic studies on *p*-type doping using tetrafluoro-tetracyano-quinodimethane (F4-TCNQ) for OSCs and OLEDs.^{38,39)} Moreover, electron-donating organic molecules such as HAT-CN₆ and CN₆-CP have also been reported as acceptor dopants.^{40,41)}

However, *n*-type doping is more challenging owing to the instability of donor dopants with respect to oxygen. Exposure to oxygen must be prevented in order to perform the *n*-type doping as oxygen acts as an acceptor. Conventionally, alkali metals such as sodium, potassium, lithium, cesium, and strontium have been used. However, the undesirable diffusion into the organic films complicates the precise fabrication of devices. Moreover, metal atoms act as recombination centers, which can significantly

affect the device characteristics. Recently, electron-donating organic molecules such as pyronin B⁴²⁻⁴⁴⁾ and AOB⁴⁵⁾ and DMBI derivatives⁴⁶⁻⁴⁹⁾ have been reported as donor dopants. Moreover, transition-metal complexes including Ru,⁵⁰⁾ Co,^{51,52)} Cr,⁵³⁾ and W⁵³⁻⁵⁵⁾ have also been reported. The air-stable cesium carbonate (Cs₂CO₃),⁵⁶⁻⁵⁸⁾ which is often used as an electron-extracting layer,⁵⁹⁾ is one of the most promising acceptor dopants. Furthermore, doping with electron-donating organic molecules such as phosphine derivatives (PhIm) has also been reported.⁶⁰⁾

In this thesis, MoO₃, Fe₂Cl₆, and Cs₂CO₃ were used owing to their high electron acceptor and donor qualities and simple handling.

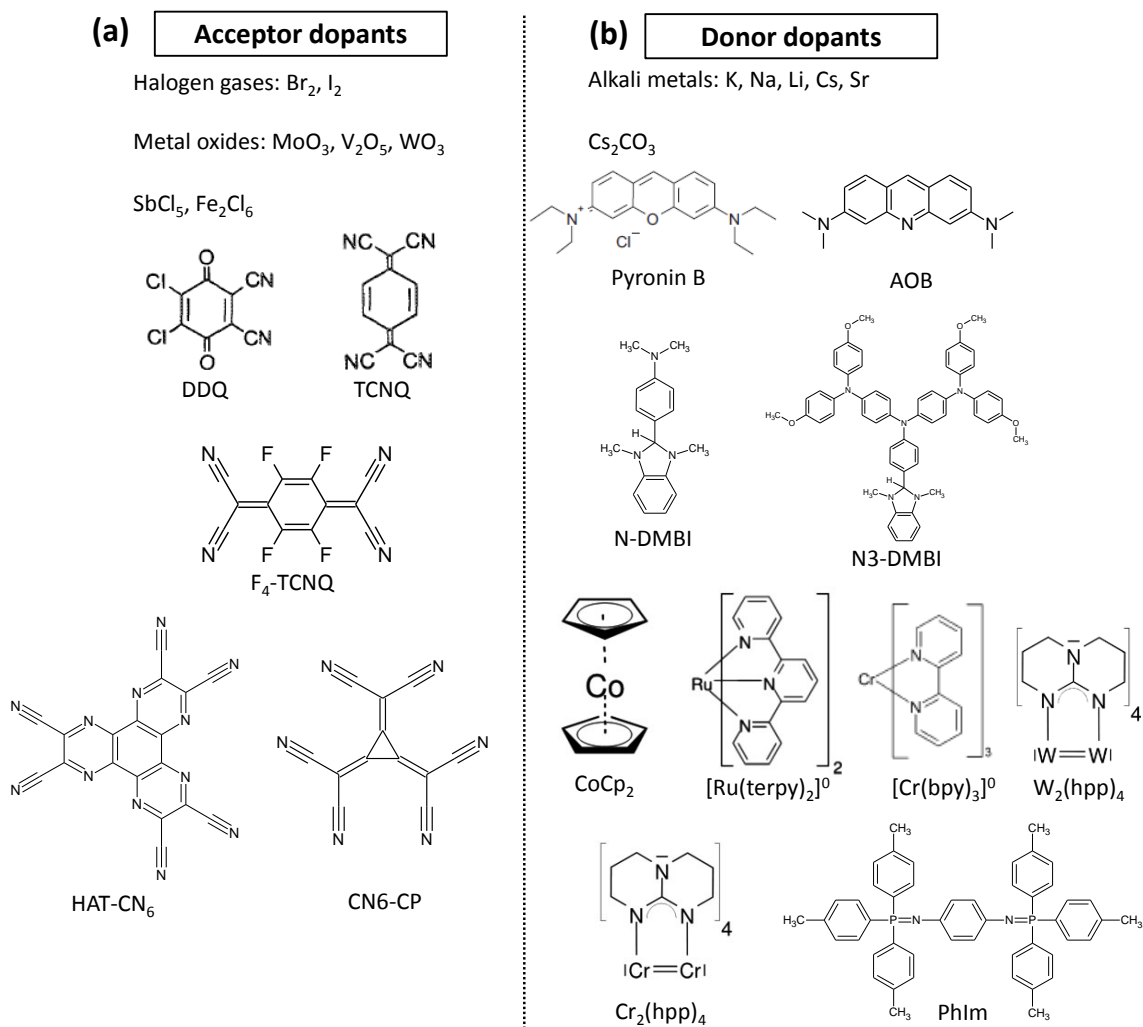


Fig. 1.6 (a) Acceptor and (b) donor dopants for organic semiconductors.

1.4.2 Mechanism of Impurity Doping

Fig. 1.7 shows schematic energy diagrams of an acceptor- and donor-doped organic semiconductor. In the case of acceptor doping, the LUMO level of the dopant (red solid line) needs to be located below the HOMO level of the organic semiconductor. The acceptor can withdraw an electron from the HOMO level of the organic semiconductor (black solid curve). On the other hand, in the case of donor doping, the HOMO level of the dopant (blue solid line) needs to be located above the LUMO level of the organic semiconductor. The donor can donate an electron to the LUMO level of the organic semiconductor (black solid curve). Therefore, CT occurs between the dopant and organic semiconductor due to the impurity doping.

Kubo et al. have confirmed that CT complexes form between fullerene (C_{60}) and various dopants.^{61,62)} Two types of CT complexes, i.e., $C_{60}^+ \cdots MoO_3^-$ and $C_{60}^- \cdots Cs_2CO_3^+$, formed in C_{60} films with acceptor (MoO_3) and donor (Cs_2CO_3) dopants (Figs. 1.8 (a) and (b)), respectively. The doped C_{60} films exhibited color changes and CT absorption. In addition, in the case of MoO_3 doping, the Fermi energy (E_F) shifted to the HOMO level. This suggests that the MoO_3 -doped C_{60} film was *p*-type. On the other hand, in the case of Cs_2CO_3 doping, E_F shifted to the LUMO level, suggesting that the Cs_2CO_3 -doped C_{60} film was *n*-type. Recently, Hiramoto et al. have reported similar shifts in E_F for various organic semiconductor films with impurity doping at a concentration of 3000 parts per million (ppm).^{11,12)} Therefore, the mechanism of the impurity doping can be explained by the CT model.

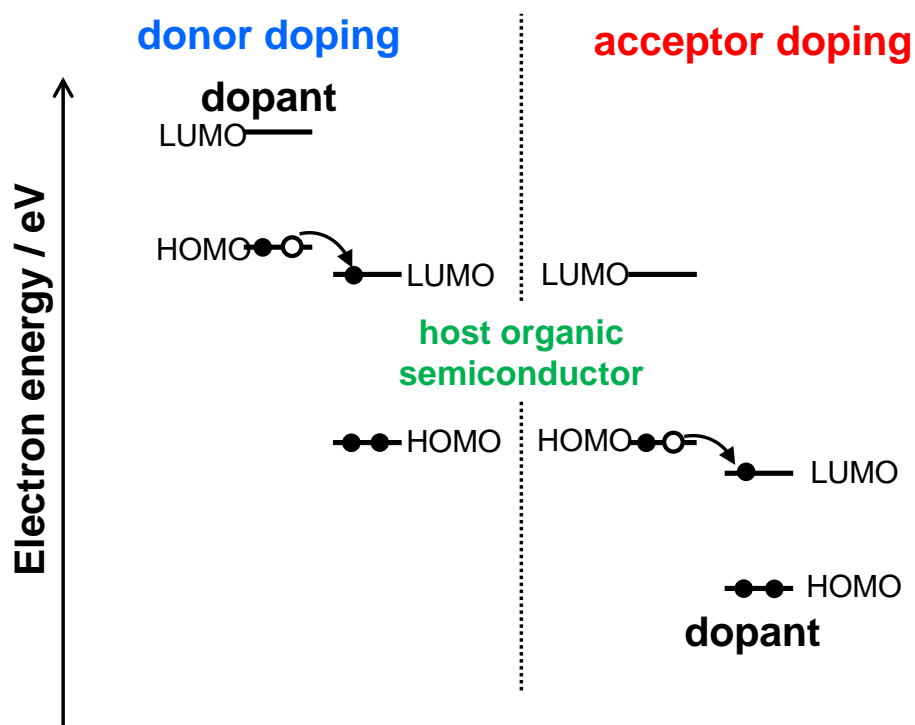


Fig. 1.7 Schematic energy band diagram of the acceptor and donor doping in an organic semiconductor.

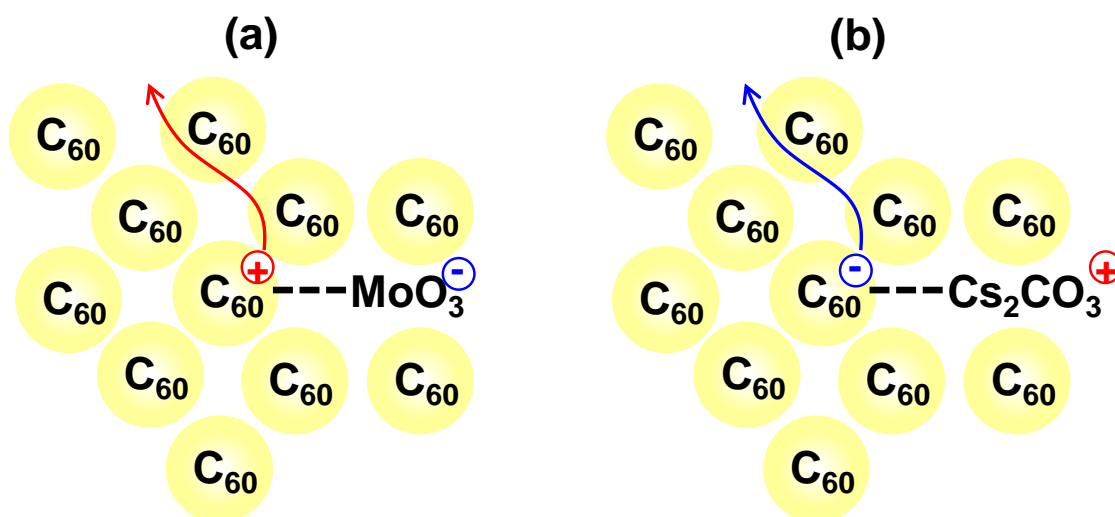


Fig. 1.8 Schematics of the (a) MoO₃- and (b) Cs₂CO₃-doped C₆₀ films.

1.5. Hall Effect Measurements for Doped Organic Single-Crystals

The carrier concentration (N) and carrier mobility (μ) of band-conducting organic semiconductors can be measured by the Hall effect. The Hall effect was discovered by Edwin Herbert Hall in 1879. Fig. 1.9 shows schematic diagrams of Hall effect measurements in a p -type organic semiconductor. When a magnetic field (B) (black mark) is applied perpendicular to the current (I) (blue solid line), a potential difference is generated between the two electrodes by the Lorentz force (green solid arrows), referred to as Hall voltage (V_H). V_H and carrier concentration per unit volume (N , cm^{-3}) can be determined by:

$$V_H = \frac{R_H I B}{d} \quad (1.5)$$

$$N = \frac{1}{R_H e} \quad (1.6)$$

where d is the thickness and R_H is the Hall coefficient.

Positive and negative R_H correspond to positive (p)- and negative (n)-type materials, respectively. In addition, not only N but also the Hall mobility (μ_H) can be determined using the Hall effect:

$$\mu_H = \sigma R_H \quad (1.7)$$

where the carrier conductivity (σ) can be measured using the van der Pauw method. Trapped carriers do not contribute to μ_H as they cannot move under the influence of the Lorentz force. Therefore, μ_H is regarded as the intrinsic mobility without trap effect.

The Hall voltage of an undoped rubrene single-crystal with band-like transport properties has been measured with the assistance of trap-healing⁶³⁾ and gate bias using a field-effect transistor (FET). In addition, our group have recently reported the Hall effect for doped organic single-crystals without the FET mechanism. In this method, as carriers are not induced from the outside, the number of carriers generated by the impurity doping can be directly observed.

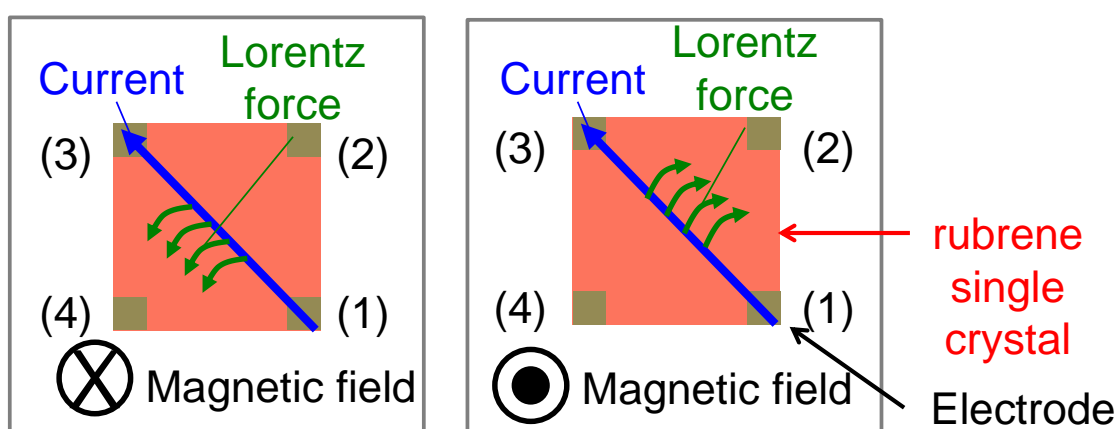


Fig. 1.9 Schematic diagrams of the Hall effect measurement.

1.6. Motivation for This Doctoral Thesis

In this doctoral thesis, the effects of lateral charge carrier transport on the performances of high-mobility organic crystalline photovoltaic cells are investigated. The main objectives of this thesis are as follows.

(i) Lateral-type OPV cells utilizing the long carrier range in high-mobility organic single-crystalline films

Blended junctions consisting of donor and acceptor molecules are indispensable for the development of OSCs. However, the thickness of a blended junction is limited owing to carrier accumulation from imperfections in the electron- and hole-transport routes formed by percolation. In this thesis, an ideal structure, i.e., a lateral alternating multilayered structure consisting of donor and acceptor molecules that satisfy both exciton collection and carrier collection requirements is proposed. Recently, organic single-crystals with high carrier mobilities (μ) (reaching $43 \text{ cm}^2\text{V}^{-1}\text{s}^{-1}$) have been reported. The high mobility observed in the direction parallel to the substrate due to strong π - π interactions is larger than the mobility required for the proposed photovoltaic cells. Therefore, in this study, lateral-type OPV cells utilizing the long carrier range in high-mobility organic single-crystalline films were fabricated.

(ii) Doped organic single-crystal photovoltaic cells

Recently, a high hole mobility ($40 \text{ cm}^2\text{V}^{-1}\text{s}^{-1}$) and large exciton diffusion length (2–8 μm) were reported for a rubrene single-crystal. Although these findings strongly suggest the suitability of organic single-crystals for photovoltaic cells, there is an obstacle related to carrier collection, which originates from the high resistivity of these

crystals owing to the absence of free carriers. On the other hand, a bulk-doping technique can be used for homoepitaxially grown rubrene single-crystal layers. This technique provides a doped high-conductivity route in organic single-crystals for carrier collection. Therefore, in this study, doped rubrene single-crystal photovoltaic cells were fabricated.

1.7. Thesis Overview

This thesis consists of six chapters.

In Chapter 1, the background on carrier transport and impurity doping in organic semiconductors is presented. The motivations for the analyses reported in this thesis are also presented.

In Chapter 2, the experimental equipment and methods are described. Plate-like organic single-crystals were grown by physical vapor transport. The photovoltaic devices were fabricated using custom-made metal masks or movable mask system. Doped organic semiconductors were fabricated using a multicomponent coevaporation technique. The deposition rates of the dopants were monitored using a quartz crystal microbalance equipped with a computer monitoring system. These rates were controlled using rotating shutters with aperture ratios of 1/10 and 1/100, which enabled control of the doping concentration to a level as low as 10 ppm.

In Chapter 3, we focus on the lateral transport and collection of electrons, employing a naphthalenetetracarboxylic dianhydride (NTCDA) single-crystal as the lateral electron transport crystal. The electron range (L_e) was determined by varying the interelectrode distance (L). When L was increased from 30 to 50 μm , the photocurrent significantly decreased; therefore, the electron range (L_e) was approximately 30 μm . The operation of single-crystal OPV cells using lateral electron transport with a macroscopic value of 30 μm was demonstrated. Based on the multiple trapping model, as L_e could be expressed by $L_e = \mu_e \tau_e E$ (μ_e : electron mobility, E : electric field), the calculated electron lifetime τ_e was 0.52 ms using $L_e = 30 \mu\text{m}$ and $\mu_e = 2.9 \times 10^{-2} \text{ cm}^2 \text{ V}^{-1} \text{ s}^{-1}$. The large τ_e close to the order of milliseconds indicates the possibility of electron ranges on the order of millimeters.

In Chapter 4, the hole range of 0.4 mm was demonstrated using a high-hole-mobility (μ_h) organic semiconductor, dioctyl-benzothieno-benzothiophene (C8-BTBT) ($\mu_h = 43 \text{ cm}^2\text{V}^{-1}\text{s}^{-1}$). In addition, the electron range of 0.2 mm was demonstrated using a high-electron-mobility organic semiconductor, dioctyl-perylenetetracarboxylic diimide (PTCDI-C8) ($\mu_e = 1.7 \text{ cm}^2\text{V}^{-1}\text{s}^{-1}$). Finally, lateral alternating multilayered junctions combining C8-BTBT and PTCDI-C8 were demonstrated. 93% of the photogenerated electrons and holes were laterally collected over a long distance (0.14 mm). The exciton diffusion length of 12 nm was obtained by changing the layer thickness from 50 to 10 nm. The exciton-collection efficiency reached 75% at the layer thickness of 10 nm. A lateral organic alternating multilayered junction, which completely collects both excitons and carriers, can be an alternative blended junction for OSCs.

In Chapter 5, doped rubrene single-crystal photovoltaic cells were fabricated. These photovoltaic cells can be regarded as function-separated devices. The *p*-doped single-crystalline layer acts as a *p*-type hole-transporting layer, the *pn*-homojunction acts as the exciton dissociator, and the single-crystal substrate acts as the exciton collector. The area dependence of the *pn*-homojunction showed that the whole photocurrent generated in the *pn*-homojunction with a macroscopic area of $2 \text{ mm} \times 1 \text{ mm}$ was collected through the *p*-doped single-crystalline layer. Therefore, the *p*-doped single-crystalline layer can be regarded as a pseudo-electrode. In addition, the analysis of the internal quantum efficiency depending on the light irradiation direction showed that the single-crystal substrate collected excitons to the *pn*-homojunction with a collection efficiency reaching 46%, owing to the large exciton diffusion length of 2.7 μm .

In Chapter 6, the conclusions of this thesis and prospects for the future are presented.

References

- 1) H. Akamatsu, H. Inokuchi, and Y. Mastunaga, *Nature.*, **173**, 168 (1954).
- 2) C. W. Tang, S. A. Vanslyke, *Appl. Phys. Lett.*, **51**, 913 (1987).
- 3) C. W. Tang, *Appl. Phys. Lett.*, **48**, 183 (1986).
- 4) W.N. Li, L. Ye, S. S. Li, H. F. Yao, H. Ade, J. H. Hou, *Adv. Mater.* 1707170 (2018).
- 5) H. Zhang, H. Yao, J. Hou, J. Zhu, J. Zhang, W. Li, R. Yu, B. Gao, S. Zhang, J. Hou, *Adv. Mater.* 1800613 (2018).
- 6) J. Takeya, K. Tsukagoshi, Y. Aoyagi, T. Takenobu, Y. Iwasa, *Jap. J. Appl. Phys.* **44**, L1393 (2004).
- 7) C. Liu, T. Minari, X. Lu, A. Kumatani, Takimiya, K. Tsukagoshi, *Adv. Mater.*, **23**, 523 (2011).
- 8) H. Xie, H. Alves, A. F. Morpurgo, *Phys. Rev. B*, **80**, 245305 (2009).
- 9) T. Sakanoue, H. Sirringhaus, *Nat. Mater.*, **9**, 736 (2010).
- 10) N. A. Minder, S. Ono, Z. Chen, A. Facchetti, A. F. Morpurgo, *Adv. Mater.*, **24**, 503–508 (2012).
- 11) M. Hiramoto, M. Kikuchi, S. Izawa, *Adv. Mater.* 1801236 (2018).
- 12) M. Hiramoto, M. Kubo, Y. Shinmura, N. Ishiyama, T. Kaji, K. Sakai, T. Ohno, and M. Izaki, *Electronics.*, **3**, 351 (2014).
- 13) B. Luussem, C.M. Keum, D. Kasemann, B. Naab, Z. Bao, and K. Leo, *Chem. Rev.*, **116**, 13714 (2016).
- 14) V. Coropceanu, J. Cornil, D. A. da Silva Filho, Y. Olivier, R. Silbey, and J. L. Bredas, *Chem. Rev.* **107**, 926 (2007).

- 15) W. Q. Deng and W. A. Goddard III, *J. Phys. Chem. B* **108**, 8614 (2004). 9G. R. Hutchison, M. A. Ratner, and T. J. Marks, *J. Am. Chem. Soc.* **127**, 16866 (2005).
- 16) E. F. Valeev, V. Coropceanu, D. A. S. Filho, S. Salman, and J. L. Bredas, *J. Am. Chem. Soc.* **128**, 9882 (2006).
- 17) S. H. Wen, A. Li, J. Song, W. Q. Deng, K. L. Han, and W. A. Goddard III, *J. Phys. Chem. B*, **113**, 8813 (2009).
- 18) J. Takeya, K. Tsukagoshi, Y. Aoyagi, T. Takenobu and Y. Iwasa, *Jpn. J. Appl. Phys.*, **44**, 1393 (2004).
- 19) C. Liu, T. Minari, X. Lu, A. Kumatani, Takimiya, K. Tsukagoshi, *Adv. Mater.*, **23**, 523 (2011).
- 20) H. Xie, H. Alves, A. F. Morpurgo, *Phys. Rev. B*, **80**, 245305 (2009).
- 21) J. Tsurumi, H. Matsui, T. Kubo, R. Häusermann, C. Mitsui, T. Okamoto, S. Watanabe, and J. Takeya., *Nat. Phys.*, **13**, 994 (2017).
- 22) T. Sakanoue, H. Sirringhaus, *Nat. Mater.*, **9**, 736 (2010).
- 23) N. A. Minder, S. Ono, Z. Chen, A. Facchetti, and A. F. Morpurgo, *Adv. Mater.*, **24**, 503 (2012).
- 24) V. Coropceanu, J. Cornil, D. A. da Silva Filho, Y. Olivier, R. Silbey, and J.-L. Bredas, *Chem. Rev.*, **107**, 926-952 (2007).
- 25) P. G. Lecomber, W. E. Spear, *Phys. Rev. Lett.*, **25**, 509 (1970).
- 26) F. W. Schmidlin, *Phys. Rev. B*, **16**, 2362 (1977).
- 27) V. Podzorov, E. Menard, A. Borissov, V. Kiryukhin, J.A. Rogers, M.E. Gershenson, *Phys. Rev. Lett.* **93**, 1–4 (2004).
- 28) C. Goldmann, C. Krellner, K. P. Pernstich, S. Haas, D. J. Gundlach, and B. Batlogg, *J. Appl. Phys.* **99**, 034507 (2006).

- 29) M. Hiramoto, K. Ihara, H. Fukusumi, and M. Yokoyama, *J. Appl. Phys.*, **78**, 7153 (1995).
- 30) G. D. Sharma, S. G. Sangodkar, and M. S. Roy, *Mater. Sci. Eng. B*, **41**, 222 (1996).
- 31) M. Kubo, K. Iketaki, T. Kaji, and M. Hiramoto, *Appl. Phys. Lett.*, **98**, 073311 (2011).
- 32) M. Kubo, T. Kaji, and M. Hiramoto, *AIP Adv.*, **1**, 032177 (2011).
- 33) M. Kröger, S. Hamwi, J. Meyer, T. Riedl, W. Kowalsky, and A. Kahn, *Org. Electron.*, **10**, 932 (2009).
- 34) M. Kubo, Y. Shinmura, N. Ishiyama, T. Kaji, and M. Hiramoto, *Appl. Phys. Express*, **5**, 092302 (2012).
- 35) M. Kubo, Y. Shinmura, N. Ishiyama, T. Kaji, and M. Hiramoto, *Mol. Cryst. Liq. Cryst.*, **581**, 13 (2013).
- 36) C. Ganzorig, and M. Fujihira, *Appl. Phys. Lett.*, **77**, 4211 (2000).
- 37) M. Maitrot, G. Guillaud, and B. Boudjema, J. J. André, and J. Simon, *J. Appl. Phys.*, **60**, 2396 (1986).
- 38) J. Blochwitz, M. Pfeiffer, T. Fritz, and K. Leo, *Appl. Phys. Lett.*, **73**, 729 (1998).
- 39) K. Walzer, B. Maennig, M. Pfeiffer, and K. Leo, *Chem. Rev.*, **107**, 1233 (2007) and references therein.
- 40) J. Niederhausen, P. Amsalem, J. Frisch, A. Wilke, A. Vollmer, R. Rieger, N. Koch, *Phys. Rev. B*, **84**, 165302 (2011).
- 41) Y. Karpov, T. Erdmann, I. Raguzin, M. Al-Hussein, M. Binner, U. Lappan, M. Stamm, K.L. Gerasimov, T. Beryozkina, V. Bakulev, D. V. Anokhin, D.A. Ivanov, F. Günther, S. Gemming, G. Seifert, B. Voit, R. Di Pietro, A. Kiriy, *Adv. Mater.*, **28**, 6003 (2016).

- 42) A. G. Werner, F. Li, K. Harada, M. Pfeiffer, T. Fritz, and K. Leo, *Appl. Phys. Lett.*, **82**, 4495 (2003).
- 43) A. Werner, F. Li, K. Harada, M. Pfeiffer, T. Fritz, and K. Leo, *Adv. Funct. Mater.*, **14**, 255 (2004).
- 44) F. Li, A. Werner, M. Pfeiffer, K. Leo, and X. Liu, *J. Phys. Chem. B*, **108**, 17076 (2004).
- 45) F. Li, M. Pfeiffer, A. Werner, K. Harada, K. Leo, N. Hayashi, K. Seki, X. Liu, and X. D. Dang, *J. Appl. Phys.*, **100**, 023716 (2006).
- 46) P. Wei, J.H. Oh, G. Dong, Z. Bao, *J. Am. Chem. Soc.*, **132**, 8852 (2010).
- 47) P. Wei, T. Menke, B.D. Naab, K. Leo, M. Riede, Z. Bao, *J. Am. Chem. Soc.*, **134**, 3999 (2012).
- 48) T. Menke, P. Wei, D. Ray, H. Kleemann, B. D. Naab, Z. Bao, K. Leo, M. Riede, *Org. Electron.*, **13**, 3319 (2012).
- 49) M. Uebe, Y. Yoshihashi, K. Noda, M. Matsubara, A. Ito, *J. Mater. Chem. C*, **6**, 6429 (2018).
- 50) C. J. Bloom, C. M. Elliott, P. G. Schroeder, C. B. France, and B. A. Parkinson, *J. Phys. Chem. B*, **107**, 2933 (2003).
- 51) C. K. Chan, F. Amy, Q. Zhang, S. Barlow, S. Marder, and A. Kahn, *Chem. Phys. Lett.*, **431**, 67 (2006).
- 52) C.K. Chan, W. Zhao, A. Kahn, and I. G. Hill, *Appl. Phys. Lett.*, **94**, 203306 (2009).
- 53) T. Menke, D. Ray, J. Meiss, K. Leo, and M. Riede, *Appl. Phys. Lett.*, **100**, 093304 (2012).
- 54) M. L. Tietze, F. Wölzl, T. Menke, A. Fischer, M. Riede, K. Leo, and B. Lüssem, *Phys. Status Solidi A*, **210**, 2188 (2013).

- 55) S. Schubert, Y. H. Kim, T. Menke, A. Fischer, R. Timmreck, L. Müller-Meskamp, and K. Leo, *Sol. Energy Mater. Sol. Cells*, **118**, 165 (2013).
- 56) N. Ishiyama, M. Kubo, T. Kaji, and M. Hiramoto, *Appl. Phys. Lett.*, **101**, 233303 (2012).
- 57) N. Ishiyama, T. Yoshioka, T. Kaji, and M. Hiramoto, *Appl. Phys. Express*, **6**, 012301 (2013).
- 58) N. Ishiyama, M. Kubo, T. Kaji, and M. Hiramoto, *Org. Electron.*, **14**, 1793 (2013).
- 59) H. Liao, L. Chen, Z. Xu, G. Li, and Y. Yang, *Appl. Phys. Lett.*, **92**, 173303 (2008).
- 60) C. Momblona, L. Escrig, E. Bandiello, E. M. Hutter, M. Sessolo, K. Lederer, J. Nimoth, and H. J. Bolink, *Energy Environ. Sci.*, **9**, 3456 (2016).
- 61) M. Kubo, K. Iketaki, T. Kaji, and M. Hiramoto, *Appl. Phys. Lett.*, **98**, 073311 (2011).
- 62) M. Kubo, T. Kaji, and M. Hiramoto, *AIP Advances.*, **1**, 032177 (2011).
- 63) B. Lee, Y. Chen, D. Fu, H. T. Yi, K. Czelen, H. Najafov and V. Podzorov, *Nat. Mater.*, **12**, 1125 (2013).

Chapter 2: Experimental Equipment and Methods

2.1. Purification of Organic Semiconductors

NTCDA (naphthalene-1,4,5,8-tetracarboxylic dianhydride) (Tokyo Chemical Industry), rubrene (5,6,11,12-Tetraphenylnaphthacene) (Tokyo Chemical Industry), C₆₀ (Frontier Carbon Co., Ltd., nanom purple TL), and H₂Pc (metal-free phthalocyanine) (Dainippon Ink & Chemicals, Inc., Fastogen Blue EP-101), were purified to 7N (99.99999%) purity by temperature gradient sublimation in a quartz furnace comprising three sections at different temperatures (Fig.2.1).¹⁾ Crude samples of the organic semiconductors were placed in the high temperature section, and highly purified millimeter-scale single crystals were grown by sublimation in the middle temperature section under N₂ flow after pre-heating. (Fig. 2.2). Impurities from the crude sample were expelled to the low temperature section. In order to obtain highly purified single crystals, the proper conditions with respect to each material are required. The detailed sublimation conditions are shown in Table 2.1. The high purity commercial products such as DBP (Tetraphenyl dibenzoperiflanthene, Luminescence Technology, sublimed grade), C8-BTBT (2,7-dioctyl[1]benzothieno[3,2-b][1]benzothiophene) (Nippon Kayaku), PTCDI-C8 (N,N'-dioctyl-3,4,9,10-perylenetetracarboxylic diimide) (Luminescence Technology, sublimed grade), BCP (bathocuproine, DOJINDO, sublimed grade), cesium carbonate (Cs₂CO₃; Aldrich, 99.995%), molybdenum trioxide (MoO₃; Alfa Aeser, 99.9995%), and iron (III) chloride (Fe₂Cl₆; Aldrich, 99.99%) were used without further purification.

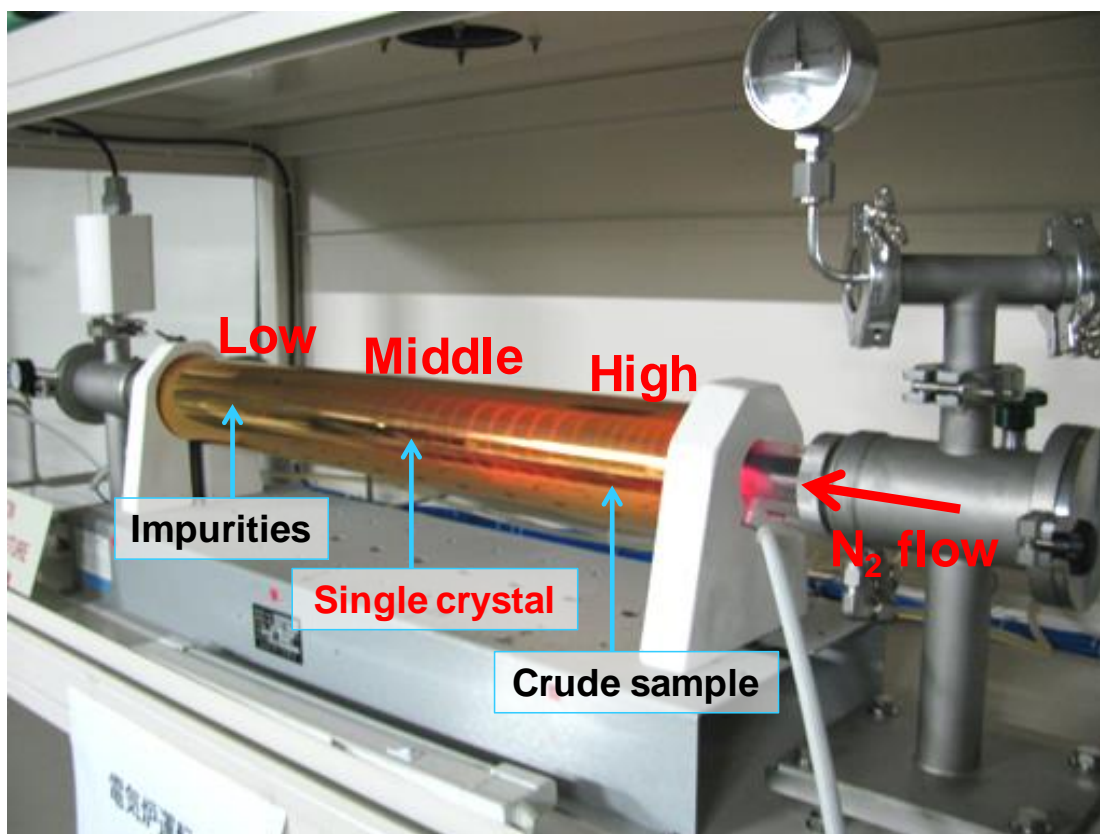


Fig. 2.1 Quartz furnace comprising three sections at different temperatures

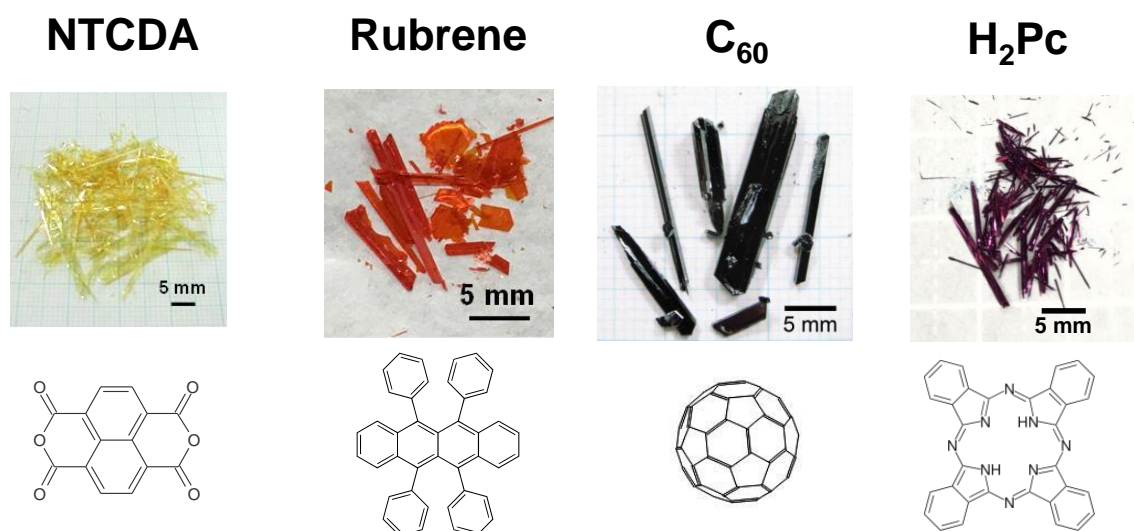


Fig. 2.2 Purified single crystals of organic semiconductors and chemical structures.

Table 2.1 Sublimation conditions for organic semiconductors.

	Temperature / °C			N ₂ flow Pressure / atm	Heating Time / h
	Low	Middle	High		
Pre-heating	150	150	150	Under vacuum	1
NTCDA	100	200	380	1	2
rubrene	170	230	325	0.1	0.5
C₆₀	310	580	745	1	36
H₂Pc	270	300	500	0.1	5

2.2. Fabrication of Organic Single Crystals for devices

NTCDA and rubrene single crystals (Fig 2.3) were grown by physical vapor transport under the conditions that thin and plate-like crystals were formed (Fig.2.1). After cooling to room temperature, the target crystal was picked up using a toothpick or tweezers or hair brush with taking advantage of a static electricity. The typical thickness of these crystals was around several microns.

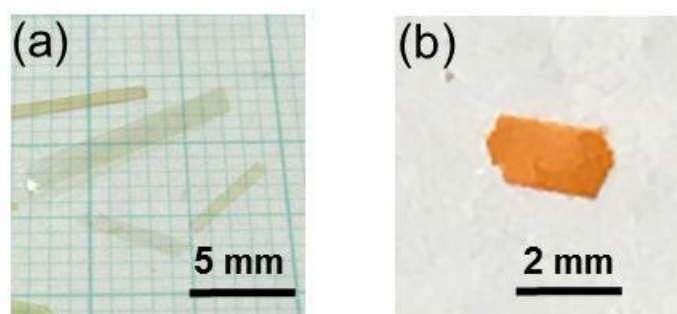


Fig. 2.3 Plate-like single crystals of (a) NTCDA and (b) rubrene.

2.3. Experimental Environment

The semiconductors were evaporated in an oil-free vacuum evaporation chamber (EpiTech Inc., ET300-6EHK) built into a glove box (UNICO, UL-1400ATW) ($\text{H}_2\text{O} < 0.7 \text{ ppm}$, $\text{O}_2 < 0.2 \text{ ppm}$) (Fig.2.4). The samples were not exposed to air at any time during either film fabrication or measurement in order to avoid effects due to moisture and oxygen.

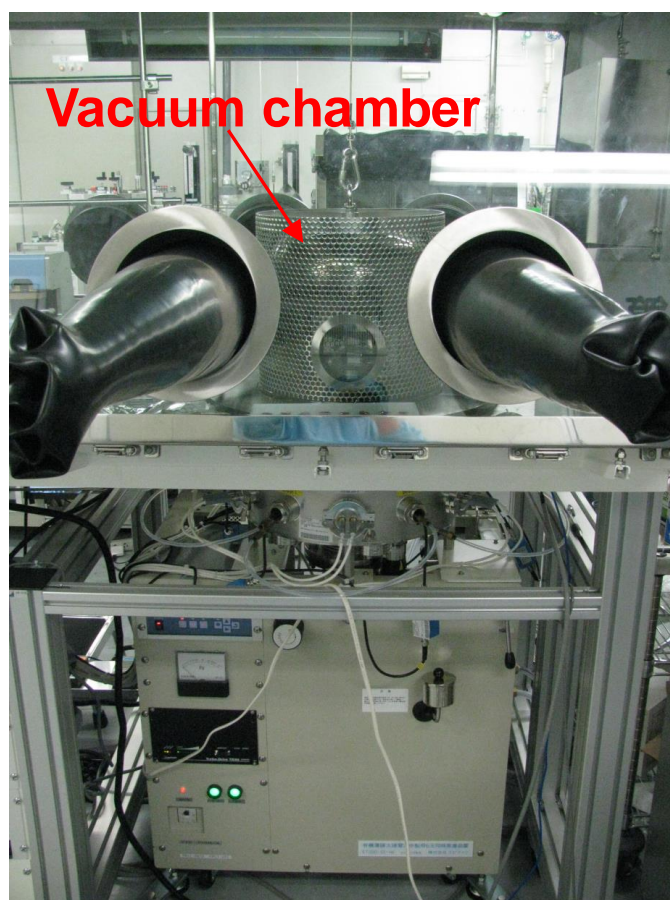


Fig.2.4 Vacuum chamber contained within a glove box.

2.4. Impurity Doping at Low Concentration for Organic Semiconductors

Impurity doping for the organic semiconductors was performed using a multi-component co-evaporation technique as shown in Fig. 2.5. The evaporation sources were prepared in Al₂O₃ pots (Nilaco, C-1). All materials were independently evaporated using tungsten basket resistance heaters (Nilaco, BH-1) under vacuum ($< 10^{-5}$ Pa). The evaporation rates were controlled using quartz crystal microbalances (QCMs) (INFICON, 750-1050-G10) connected to a computer monitoring system (ULVAC, CRTM-9000G/Depoview). The monitored thickness was calibrated using a tooling factor that can be calculated by measuring the actual film thickness using a surface profiler (Veeco, Dektak150).

Fig. 2.6 shows an example of the dependence of the film thickness of the dopant on the evaporation time. The evaporation rate can be determined from the slope of the baseline (1.0×10^{-5} nm s⁻¹). The observed cyclic fluctuations were caused by temperature variations in the coolant water for the QCMs. When the host organic semiconductor evaporates at 0.1 nm s⁻¹, the ratio of the evaporation rate of dopant to that of host organic semiconductor gives a doping concentration of 100 ppm. Moreover, extremely low doping concentrations of below 10 ppm were realized by reducing the dopant evaporation rate using rotating disks containing slits with aperture ratios of 1:10 or 1:100. In addition, in order to grow homoepitaxial films on the rubrene single crystal substrate, rubrene was evaporated at a low evaporation rate of 3.3×10^{-3} nm s⁻¹ at room temperature. The minimum evaporation rate of 3.3×10^{-8} nm s⁻¹ for 10 ppm doping could be realized by using the rotating disk.

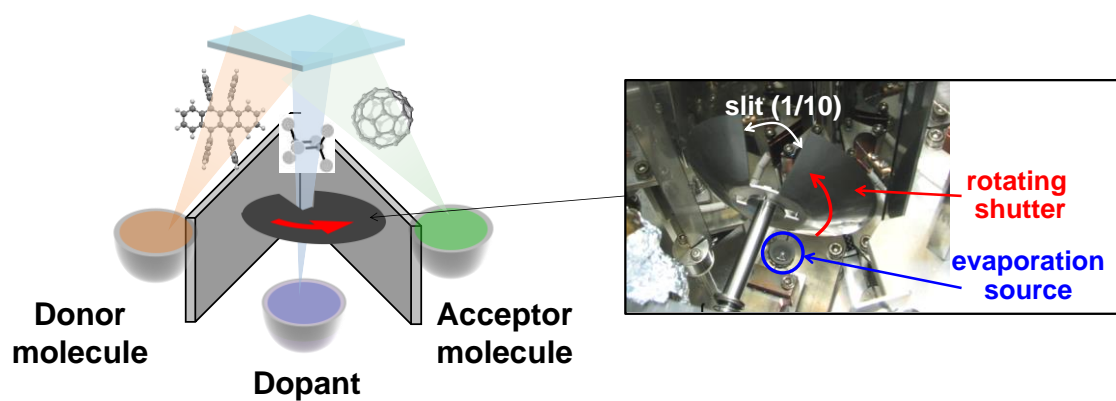


Fig. 2.5 Schematic illustration of coevaporation for doping of organic semiconductors.

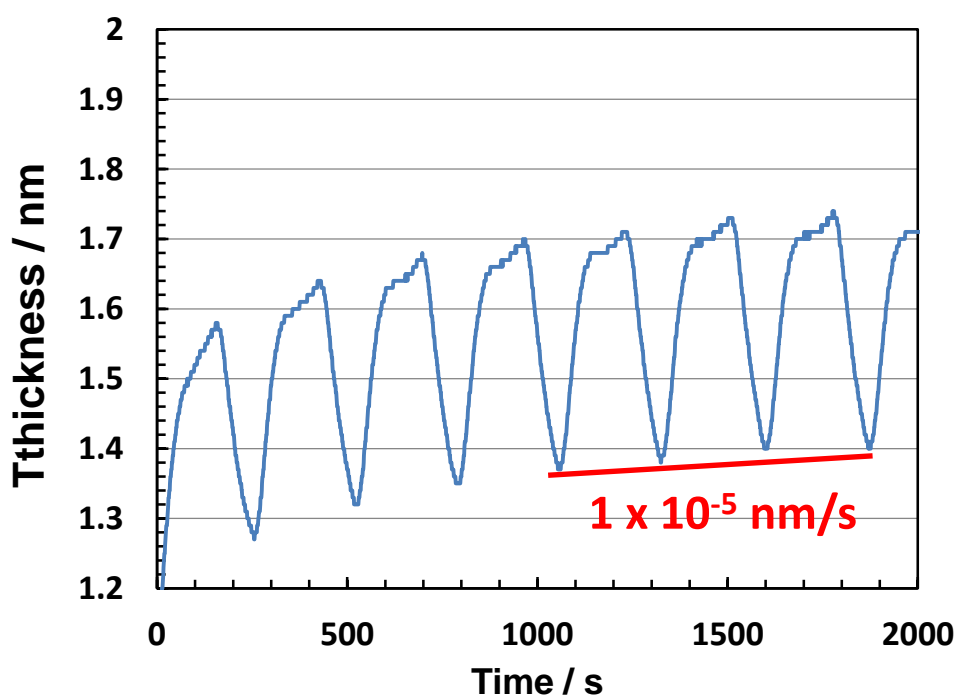


Fig. 2.6 Monitored evaporation thickness vs. evaporation time.

2.5. Fabrication of devices

2.5.1 Lateral type Organic Single Crystal Photovoltaic cells (chapter 3 and 5)

NTCDA and rubrene single crystals (Fig 2.3) were grown by physical vapor transport under the conditions that thin and plate-like crystals were formed. Metal masks were used for separating the hole and electron collecting electrodes. In chapter 3, metal masks with pairs of square apertures separated by distances of 20, 30, 50, and 100 μm were used (Fig. 2.7 (a)). In chapter 5, Metal masks with pair of rectangles, which area is 2 mm \times L mm, were used (Fig. 2.7 (b)). The lateral gap between the two electrodes was kept at 0.05 mm. The value of L was varied from 0.2 to 1.0 mm.

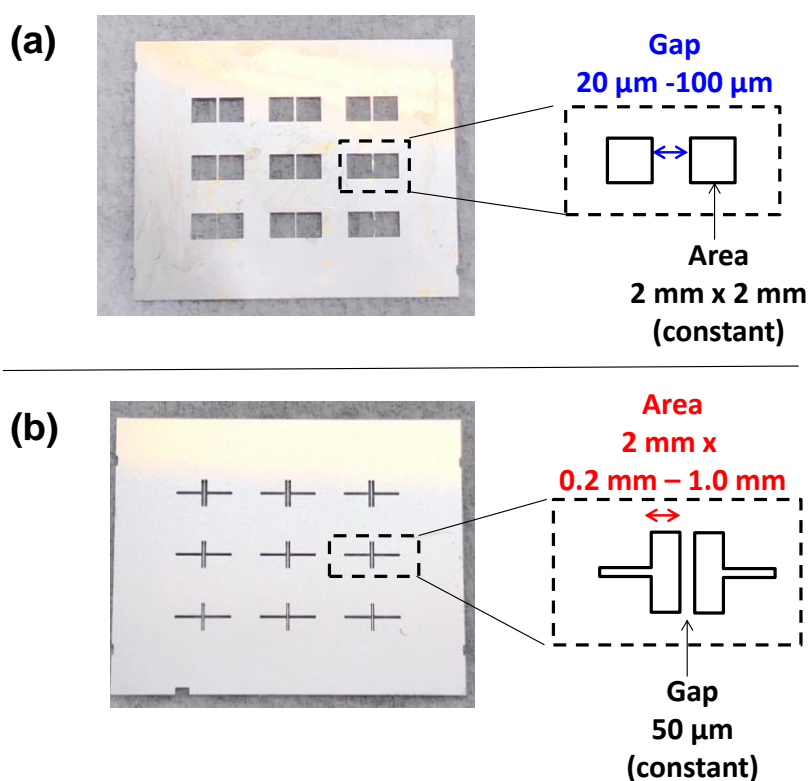


Fig.2.7 (a) Metal masks with pairs of square apertures separated by distances of 20, 30, 50, and 100 μm . (b) Metal masks with pair of rectangles which area is 2 mm \times L mm.

2.5.2 Lateral Alternating Multilayered Junctions for Organic Solar Cells (chapter 4)

For the lateral alternating multilayered junction cells (Fig. 2.8), C8-BTBT, acting as the hole pathway, and PTCDI-C8, acting as the electron pathway, were vacuum deposited alternately on sapphire substrate. Each layer thickness of the C8-BTBT and PTCDI-C8 films was decreased from 50 to 25 to 10 nm while keeping the thickness of the C8-BTBT and PTCDI-C8 films the same. The total thickness of the multilayered junction was maintained at 100 nm. The C8-BTBT and PTCDI-C8 films were selectively connected to only the hole- and electron-collecting electrodes, respectively, by using a customized movable mask system (EpiTech, Inc.) (Fig. 2.9).

A sapphire substrate set on the mask (Fig. 2.10, right upper) was slid by a precise positioning system from side-to-side along the direction of the red double arrow. C8-BTBT, PTCDI-C8, the hole-collecting electrode (MoO_3/Ag), and the electron-collecting electrode (BCP/Ag) were deposited through the apertures in the order of the aperture number, i.e., (1), (2), (3), and (4), respectively. To prepare the superlattice, evaporation through apertures (1) and (2) was repeated. The cell area ($7.7 \times 10^{-3} \text{ cm}^2$) is defined by the length of the overlap of C8-BTBT and PTCDI-C8 (0.014 cm) and the electrode width (0.57 cm).

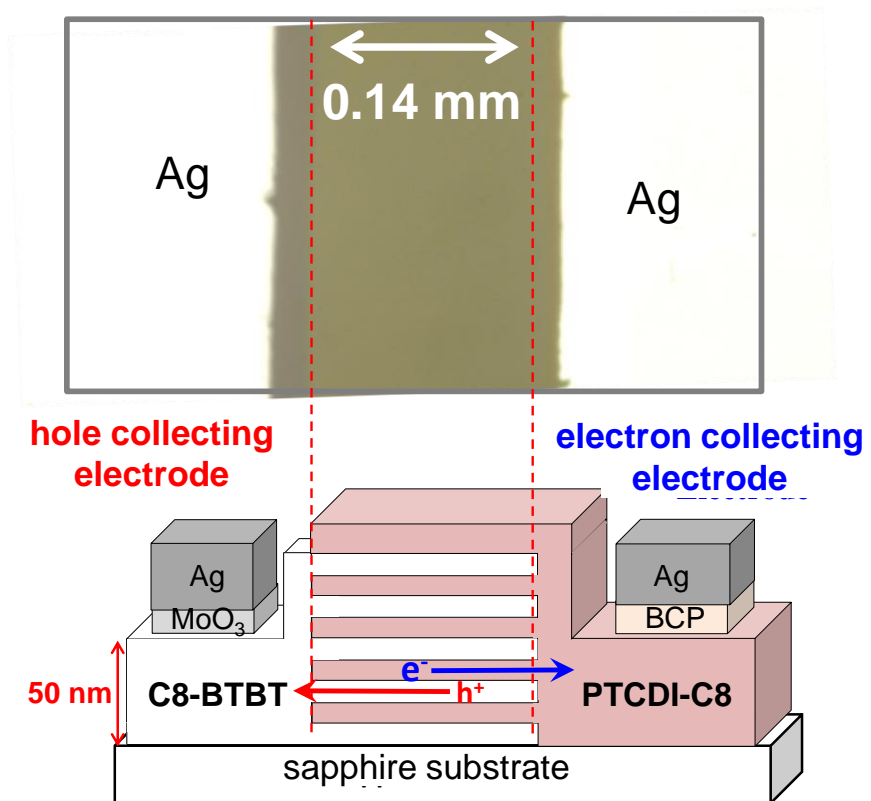


Fig.2.8 A photograph and the corresponding structure of the lateral alternating multilayered junction..

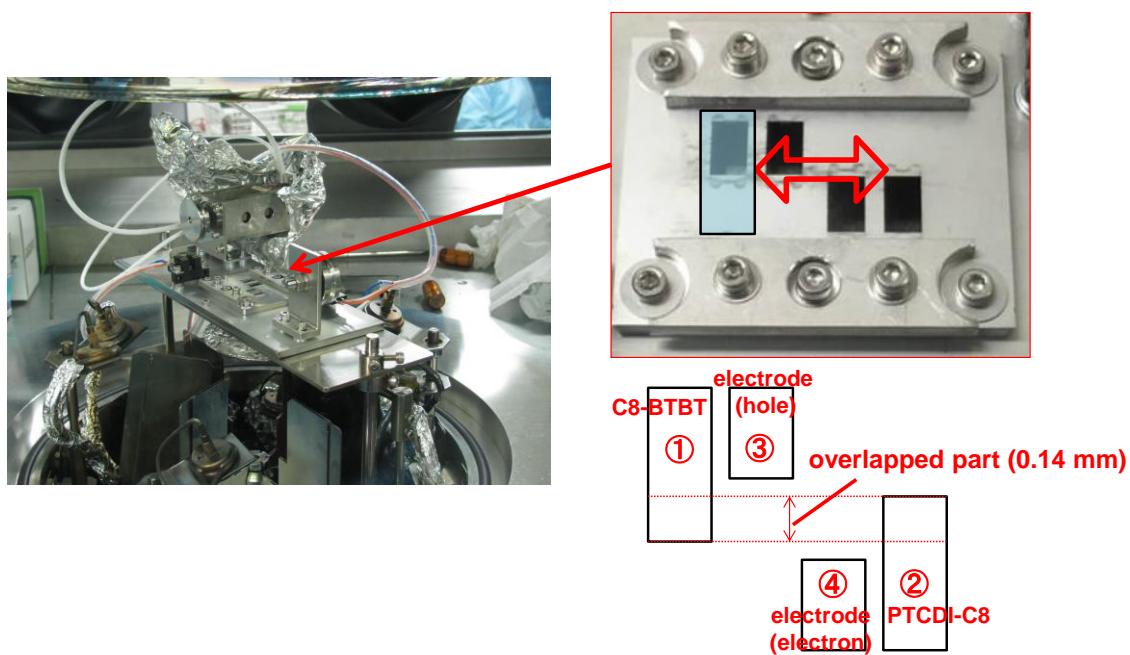


Fig.2.9 A photograph and an illustration of a customized movable mask system.

2.6 Measurements of Photovoltaic Properties

2.6.1 General

All the samples were set to into a vacuum sample container with a quartz glass window in order to measure the photovoltaic properties without exposing to the atmosphere (Epi Tech Inc.) (Fig. 2.10) During the measurement, the pressure inside the container was kept at 10^{-3} Pa.

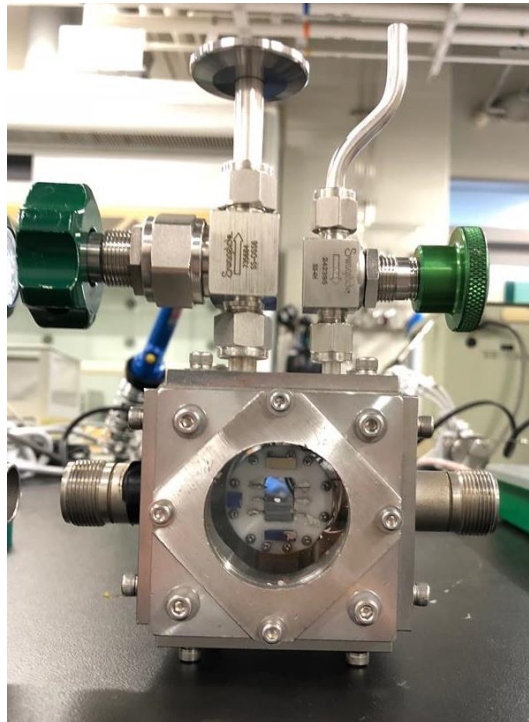


Fig. 2.10 Vacuum sample container with a quartz glass window. Simulated solar light can be irradiated from both side of this container.

2.7.2. Current Density-Voltage (*J-V*) Characteristics

The current density-voltage (*J-V*) characteristics were measured by irradiating the cell with simulated solar light (USHIO INC., MS110AAA) (AM1.5, 100 mW cm⁻²) (Fig. 2.11). Fig. 2.12 shows typical current-voltage (*J-V*) characteristics in the dark and under irradiation with the simulated solar light. The voltage was swept from -1.0 to 1.0 V at 0.1 V · s⁻¹. The photocurrent density at 0 V and the voltage at 0 mAcm⁻² are defined as the short-circuit current density (J_{sc}) and the open-circuit voltage (V_{oc}), respectively. The power conversion efficiency (η_p), i.e., the ratio of the maximum power that the cell can produce (P_{max}) to the incident light intensity (P_{in}), is given by the following equation (Eq.2.3).

$$\eta_p = \frac{P_{max}}{P_{in}} = \frac{J_{sc} \cdot V_{oc} \cdot FF}{P_{in}} \quad (2.3)$$

The fill factor (FF) is the ratio of the maximum power (red shaded rectangle, Fig. 2.12) to the product of J_{sc} and V_{oc} (dashed line rectangle, Fig. 2.12) (Eq. 2.4).

$$FF = \frac{P_{max}}{J_{sc} \cdot V_{oc}} = \frac{J_{max} \cdot V_{max}}{J_{sc} \cdot V_{oc}} \quad (2.4)$$

J_{max} and V_{max} are the current density and voltage at the maximum power output. FF signifies how close the *J-V* curve is to a step function. The closer the curve is to a step function, the larger the power that can be extracted.

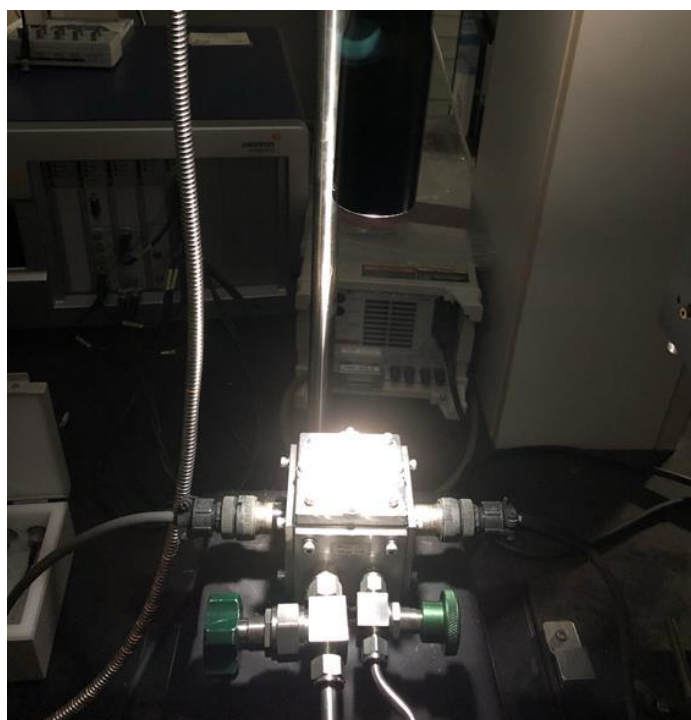


Fig. 2.11 J-V measurement with a solar simulator.

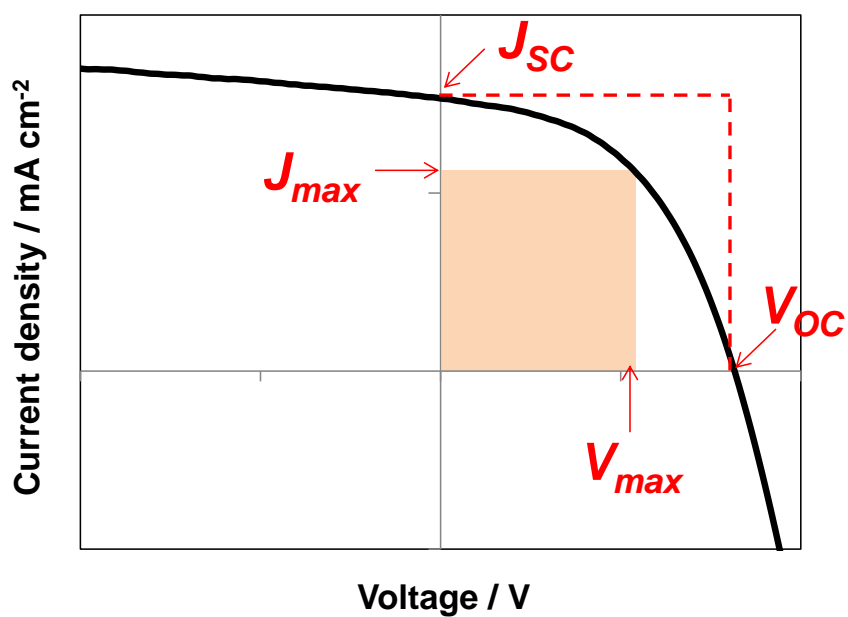


Fig. 2.12 J-V characteristics under light irradiation.

2.7.3. Action Spectrum

The action spectrum is the incident photon to current conversion efficiency versus wavelength. Figure 2.13 shows the system used for measuring the action spectra. Monochromatic light from a Xe-lamp (Shimadzu, SPG-3ST) is passed through a monochromator and used to irradiate the photovoltaic cell. The difference between the photocurrent and the dark current, i.e., the number of carriers collected, was measured from 900 to 300 nm in intervals of 20 nm under short-circuit conditions. The number of incident photons was determined by the same measurement using a standard silicon diode (Hamamatsu Photonics, S1337-66BQ). The external quantum efficiency (EQE) was determined from the ratio of the number of carriers collected to the number of incident photons.

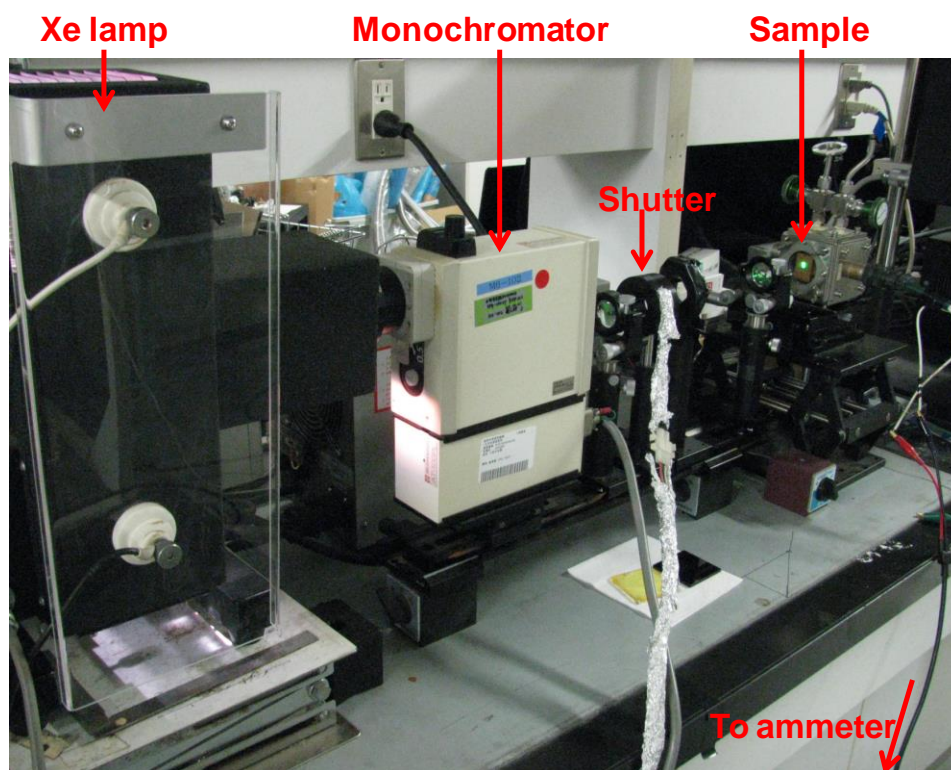


Fig. 2.13 Action spectrum measurement system.

2.7 Hall effect Measurement

A Hall effect⁸⁻¹⁰⁾ and specific-resistance measurement system (Toyo Corp., ResiTest 8300) was employed as shown in Fig 2.14. The samples were fabricated on quartz substrates. Electrodes were evaporated onto the organic thin films through a metal mask with a distance between the electrodes (50 μm). To prepare ohmic contacts, heavily doped layers were fabricated beneath the electrodes.¹¹⁾

Fig. 2.15 shows a typical example of the variation of the Hall voltage with the magnetic field. The Hall voltage (V_H) is obtained from the amplitude, as shown in the figure. The carrier concentration per unit volume (N , cm^{-3}) and mobility ($\text{cm}^2\text{V}^{-1}\text{s}^{-1}$) were determined by the observed R_H (detail in chapter 1.5).

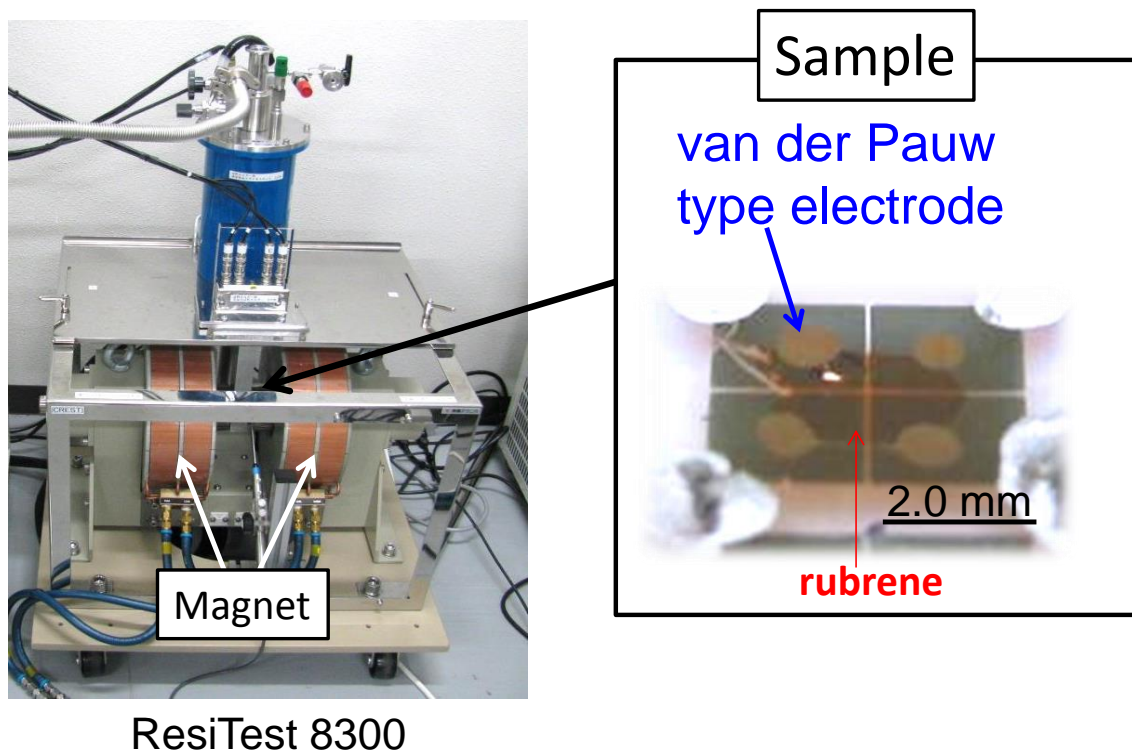


Fig. 2.14 Hall-effect measurement using the van der Pauw method

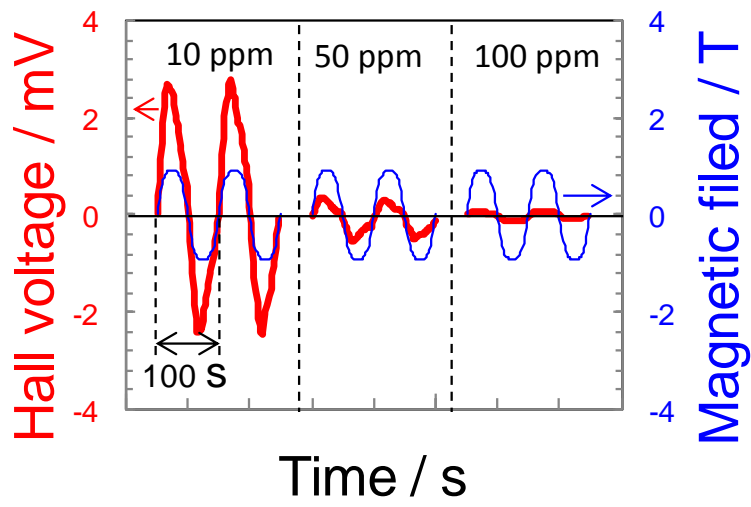


Fig. 2.15 Hall voltage with the magnetic field at the various doping concentrations.

2.8 References

- 1) R.A. Laudise, Ch. Kloc, P.G. Simpkins, and T. Siegrist, *J. Cryst. Growth.*, **187**, 449 (1998).
- 2) M. Hiramoto, M. Kubo, Y. Shinmura, N. Ishiyama, T. Kaji, K. Sakai, T. Ohno, and M. Izaki, *Electronics.*, **3**, 351 (2014).
- 3) J. Endo, T. Matsumoto, and J. Kido, *Jpn. J. Appl. Phys.*, **41**, 358 (2002).
- 4) Y. Shinmura, Y. Yamashina, T. Kaji, and M. Hiramoto, *Appl. Phys. Lett.*, **105**, 183306 (2014).
- 5) M. Kubo, Y. Shinmura, N. Ishiyama, T. Kaji, and M. Hiramoto, *Mol. Cryst. Liq. Cryst.*, **581**, 13 (2013).
- 6) M. Kubo, T. Kaji, and M. Hiramoto, *Appl. Phys. Lett.*, **103**, 263303 (2013).
- 7) X. Zeng, L. Wang, L. Duan, and Y. Qiu, *Crystal Growth & Design.*, **8**, 1617 (2008).
- 8) V. Podzorov, E. Menard, J. A. Rogers, and M. E. Gershenson, *Phys. Rev. Lett.*, **95**, 226601 (2005).
- 9) J. Takeya, K. Tsukagoshi, Y. Aoyagi, T. Takenobu and Y. Iwasa, *Jpn. J. Appl. Phys.*, **44**, 1393 (2004).
- 10) K. Noda, A. Sugawara, T. Wakahiki, K. Okamoto, T. Kiyosu, K. Matsushige, and Y. Wada, *IEEJ Trans. EIS.*, **132**, 1398 (2012).

Chapter 3:

Single Crystal Organic Photovoltaic Cells Using Lateral Electron Transport

“Single Crystal Organic Photovoltaic Cells Using Lateral Electron Transport”

*Mitsuru Kikuchi, Kenichiro Takagi, Hiroyoshi Naito, *Masahiro Hiramoto,
Org. Electron., **41**, 118-121(2017).

Abstract

The operation of single crystal organic photovoltaic cells using lateral electron transport was demonstrated. The spacing between the collection electrodes, which is determined by the lateral range of the electrons, was estimated to be 30 μm . The possibility of electron ranges of the millimeter order was indicated.

3.1. Introduction

Recently, organic single crystal materials with high carrier mobilities greater than $10 \text{ cm}^2\text{V}^{-1}\text{s}^{-1}$ have been reported.¹⁻⁴⁾ Such high mobility was observed for carriers moving laterally through the material due to π - π stacking parallel to the crystal surface. Conventional organic solar cells are built vertically on indium tin oxide (ITO) glass substrates with a sandwich-type structure.⁵⁻⁸⁾ However, the thickness of such solar cells with blended layers of donor (D) and acceptor (A) molecules is limited to just around 100 nm due to the problem of carrier collection arising from imperfections in the electron and hole transport routes in the blended layer. If the photogenerated electrons and holes can be transported laterally and collected, we can be freed from the vertical transport of carriers and, as a result, freed from the limitation to the vertical thickness of the cell. Based on these considerations, we attempted to fabricate lateral type organic photovoltaic cells using high mobility organic single crystals. Initially, we focused on the lateral transport and collection of electrons.

The concept of the lateral type cell is shown in Fig. 1(b) (right). Electrons move laterally through the single crystal substrate. A pair of electrodes separated by a distance L is deposited in parallel on the crystal surface. A layer of organic semiconductor acting as a donor is inserted between the organic single crystal substrate, which acts as an acceptor, and the electrode for collecting holes. At the D/A interface, excitons dissociate into electrons and holes under light irradiation. Since the photogenerated holes move in the vertical direction, the distance to the electrode is equal to the film thickness of 30 nm. On the other hand, since the photogenerated electrons move laterally, the inter-electrode distance (L) is at least 30 μm . Thus, the lateral distance is 1000 times the vertical distance, which means that the cell

characteristics are dominated by the electron transport. The right hand edge of the hole collection electrode can be regarded as the starting point for the electrons (broken blue line). The range of the electrons (L_e) is expressed by equation (1).

$$L_e = \mu_e \tau_e E \quad (1)$$

Here, μ_e , τ_e , and E are the electron mobility, the electron lifetime, and the electric field, respectively. As shown in Fig. 3.1(b), the inter-electrode distance L can be varied. When L is within the range L_e ($L_e > L$) the electrons can be collected at the electrode, but when it is not ($L_e < L$) they cannot. So, the photocurrent should decrease when L is at around L_e . Conversely, L_e can be determined by observing the sudden drop in photocurrent.

In this study, we adopted single crystal of naphthalenetetracarboxylic dianhydride (NTCDA, Fig. 3.1(a)) for the electron transporting material for two reasons. (i) NTCDA is a well known electron transporting organic semiconductor and its use as an extremely thick (2 μm) electron transport layer in organic solar cells has been reported.⁹⁾ (ii) NTCDA single crystal is transparent in the visible region. This allows direct irradiation of the D/A interface. The charge separation energy relationship is shown in Fig. 3.1(c) and electrons are photogenerated only beneath the hole collection electrode. Hence the starting point for electrons is aligned with the right hand edge of the hole collection electrode.

Here, we demonstrate lateral electron transport and electron collection in organic photovoltaic cells comprising NTCDA single crystal.

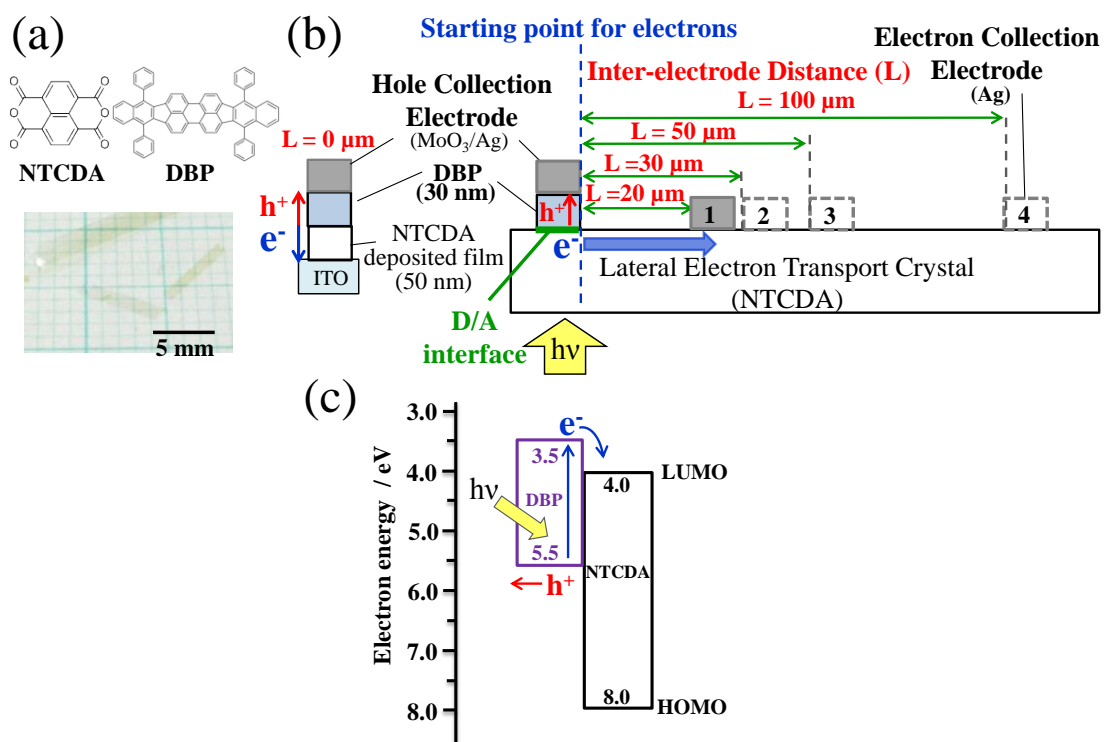


Fig.3.1 (a) Chemical structures of NTCDA and DBP. A photograph of NTCDA single crystal is also shown. (b) Configurations of the lateral cell (right) and the vertical cell (left). Thickness of NTCDA single crystal in the lateral cell and that of vacuum deposited NTCDA film in the vertical cell are 50 μm and 50 nm, respectively. (c) Energy diagrams for DBP and NTCDA.

3.2. Experimental

NTCDA (Tokyo Chemical Industry) single crystals were grown by physical vapor transport¹⁰⁾ in N₂ (1 atm) using train sublimation apparatus (EpiTech, 06ET12004). Plate shaped transparent crystals with the sizes of around 2 mm x 5 mm and thicknesses of around 50 μm were obtained (Fig. 3.1(a)). NTCDA molecules stack in a herringbone structure in single crystal having a monoclinic lattice. Detailed crystal structure was reported in ref. 11. Tetraphenyl dibenzoperiflanthene (DBP) (Fig. 3.1(a), Luminescence Technology Corp., sublimed) and MoO₃ (Alfa Aesar, 99.9995%) were used without further purification. Figure 3.1(b) (right) shows the configuration of the NTCDA single crystal cell employing lateral electron transport and collection. DBP, MoO₃, and Ag were deposited at 10⁻⁶ Pa in an oil-free vacuum evaporator (EpiTech, VTS-350M/ERH) built in a glove box purged with N₂ gas. Metal masks with pairs of square apertures separated by distances of 20, 30, 50, and 100 μm were used to form the electrode pairs. A 30 nm-thick layer of DBP and a MoO₃ (10 nm)/Ag (100 nm) hole collection electrode were deposited on the NTCDA single crystal through one of the apertures. Then an electron collection electrode (Ag (100 nm)) was deposited through the other aperture. For reference, a vertical cell (Fig. 3.1(b) (left)) was fabricated on an ITO substrate. This can be regarded as a standard cell with L = 0.

The current – voltage (J – V) characteristics were measured under irradiation of simulated solar light with intensities of 1, 8, and 10 suns (Asahi Spectra, HAL-320). Irradiation was done through the NTCDA single crystal under vacuum. The photocurrent action spectra were measured under irradiation of monochromatic light through a monochromator (Simadzu, SPG-100ST). The field-effect electron mobility

of the NTCDA single crystal was measured by putting the crystal on an n^+ -Si/SiO₂ substrate acting as a gate electrode.

3.3. Results and Discussion

Figure 3.2(a) shows the J–V characteristics of a lateral type solar cell with $L = 30 \mu\text{m}$ at solar light intensities of 1, 8, and 10 suns. The photocurrent is shown in the first quadrant. Open-circuit voltage (V_{OC}) values of 0.42, 0.62, and 0.61 V were observed for intensities of 1 (blue curve A), 8 (orange curve B), and 10 suns (green curve C). For the vertical type cell (Fig. 3.1(b)), V_{OC} values of 0.61, 0.66, and 0.67 V (see Fig. 3.3(a), broken black curve E) were observed under the same light intensities. The magnitudes of V_{OC} for the lateral cell ($L = 30 \mu\text{m}$) were slightly smaller compared to the vertical cell ($L = 0 \mu\text{m}$). This is a clear demonstration of operation of the lateral cell having an extremely long electron transport distance of $30 \mu\text{m}$.

Fig. 3.2(b) shows the action spectrum (blue dots) of the external quantum efficiency (EQE) of the short-circuit photocurrent (J_{SC}) for the lateral cell. The sensitivity of the action spectrum is aligned with the absorption spectrum of the DBP film (purple curve). When the DBP layer, which acts as a donor, was removed, no photocurrent was observed throughout the spectral range (not shown). Apparently, without the DBP/NTCDA (D/A) interface, no excitons were formed and no carriers generated. Thus, we concluded that only excitons generated in the DBP layer dissociated at the D/A interface (Fig. 3.1(c)), i.e., electrons and holes were generated only at the D/A interface. So, we can regard the right hand edge of the D/A interface as the starting point for the electrons (Fig. 1(b), broken blue line).

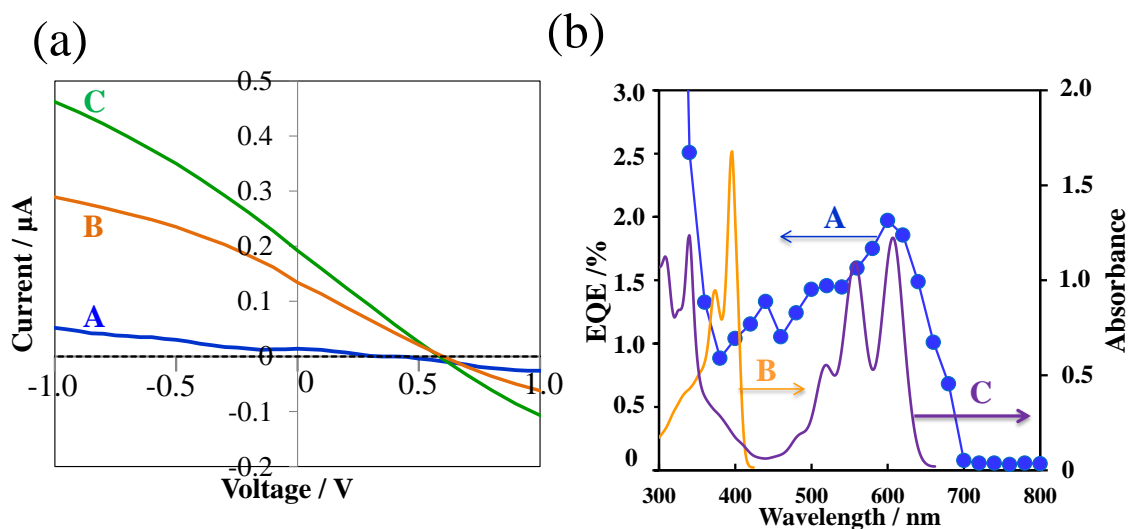


Fig. 3.2 (a) Current–voltage (J–V) characteristics at irradiation intensities of 1 sun (blue curve A), 8 suns (orange curve B), and 10 suns (green curve C). The broken black curve is the dark current. (b) Action spectrum of the external quantum efficiency (EQE) of JSC for the lateral cell (blue dots A). The solid curves are the absorption spectra of the NTCDA film (50 nm)(yellow curve B) and the DBP film (30 nm)(purple curve C).

In order to determine the electron range (L_e), the inter-electrode distance (L) was varied as shown in Fig. 3.1(b). Fig. 3.3(a) shows the J-V characteristics of cells with $L = 20, 30, 50, 100 \mu\text{m}$ under irradiation of 10 suns. When L increases from 20 (orange curve A) to 30 μm (red curve B), the magnitudes of photocurrents in the saturated region of reverse direction from -1 to -3 V coincided well. When L increases from 30 (red curve B) to 50 μm (blue curve C), the photocurrent decreases significantly. A further increase of L from 50 (blue curve C) to 100 μm (green curve D) causes a further, moderate decrease in photocurrent. This result suggests that the effective electron transport occurred within 30 μm in the lateral direction, i.e., the electron range (L_e) was around 30 μm . Since the electric field (E) depends on L , to evaluate L_e precisely, the photocurrent should be plotted as a function of L at constant E . E was determined from $E = (V_{\text{OC}} + V_{\text{appl}})/L$ where V_{appl} is the externally applied voltage. In Fig. 3(b), the photocurrent- L relationships at constant values of E of 1, 2, 3, 4, and 5 $\times 10^2 \text{ V cm}^{-1}$, which are around the magnitude of the built-in field ($2 \times 10^2 \text{ V cm}^{-1}$) estimated by $V_{\text{OC}} (0.6 \text{ V})/L (30 \mu\text{m})$, are shown.¹²⁾ Again, sharp decreases in photocurrent were confirmed between $L = 30$ and 50 μm . Photocurrent was almost constant below $L = 30 \mu\text{m}$ under the sufficient electric fields (green dots C, blue dots D, purple dots E). Therefore, we concluded that the electron range (L_e) is around 30 μm .

Fig. 3.3(c) shows schematic illustrations of lateral cells with $L = 30, 50,$ and 100 μm . L_e is 30 μm . When $L_e < L$, a small number of electrons can reach the collection electrode. This situation is realized for $L = 50$ (Fig. 3.3(c), middle) and 100 μm (Fig. 3.3(c), bottom). When $L_e > L$, most of the electrons can reach the collection electrode. This situation is realized for $L = 30 \mu\text{m}$ (Fig. 3.3(c), top).

Based on equation (1), electron lifetime τ_e was calculated to be 0.52 ms using $L_e = 30 \mu\text{m}$. Here, the electron mobility μ_e of the NTCDA single crystal was determined to be $2.9 \times 10^{-2} \text{ cm}^2 \text{ V}^{-1} \text{ s}^{-1}$ from the field-effect transistor measurement and the built-in field for the lateral cell with $L = 30 \mu\text{m}$ was used for the value of E ($2 \times 10^2 \text{ V cm}^{-1}$).¹²⁾ The value of τ_e obtained (0.52 ms) is of the order of milliseconds, and would enable an electron range L_e of the order of millimeters to be obtained if single crystal organic materials with an electron mobility μ_e of $1 \text{ cm}^2 \text{ V}^{-1} \text{ s}^{-1}$ were used. There is a strong probability of achieving millimeter order L_e since an electron mobility of $1.7 \text{ cm}^2 \text{ V}^{-1} \text{ s}^{-1}$ has already been reported for a perylene derivative.¹³⁾

It should be noted that, in the lateral cell, the active area for generating photocurrent is only in the vicinity of the right hand edge of the hole collection electrode (Fig. 3.1(b)). The maximum photocurrent density obtained for the lateral cell is comparable to that for the vertical reference cell (Fig. 3.1(b), $L = 0 \mu\text{m}$). The shape of J-V curve for vertical reference cell (Fig. 3(a), broken black curve E) coincided well to that for lateral type cell (Fig. 3.3(a), orange curve A). This strongly suggests that the photocurrent density of lateral type cell ($L = 20 \mu\text{m}$) reached that of vertical reference cell ($L = 0 \mu\text{m}$). Based on this comparison, we can calculate the width of active area for generating photocurrent in the vicinity of the right hand edge of the hole collection electrode (Fig. 3.1(b)) to be $8 \mu\text{m}$.

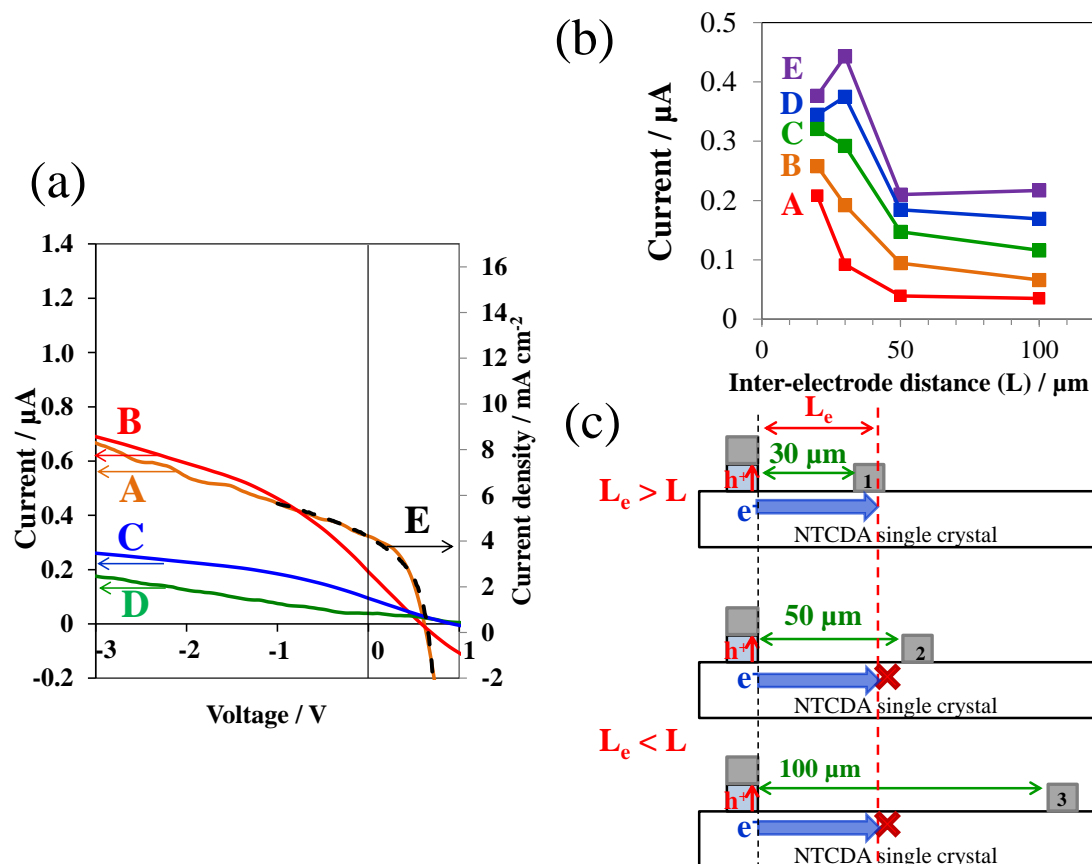


Fig. 3.3 (a) J–V characteristics of lateral cells with $L = 20 \mu\text{m}$ (orange curve A), $30 \mu\text{m}$ (red curve B), $50 \mu\text{m}$ (blue curve C), and $100 \mu\text{m}$ (green curve D) and that of the vertical reference cell (broken black curve E) under irradiation of 10 suns. (b) Dependence of the photocurrent on L at constant values of E of 1×10^2 (red dots A), 2×10^2 (orange dots B), 3×10^2 (green dots C), 4×10^2 (blue dots D), and $5 \times 10^2 \text{ V cm}^{-1}$ (purple dots E). (c) Schematic illustrations of the relationship between L and L_e in the lateral cells.

3.4. Conclusion

In conclusion, the operation of a lateral electron transport organic photovoltaic cell using NTCDA single crystal was successfully demonstrated. An electron range (L_e) of 30 μm , which determines the maximum electrode distance, was suggested. The large value of τ_e close to the order of a millisecond indicates the possibility of having electron ranges of the order of millimeters.

3.5. References

- 1) J. Takeya, M. Yamagishi, Y. Tominari, R. Hirahara, Y. Nakazawa, T. Nishikawa, T. Kawase, T. Shimoda, and S. Ogawa, *Appl. Phys. Lett.*, **90**, 1021120 (2007).
- 2) S. Haas, Y. Takahashi, K. Takimiya, and T. Hasegawa, *Appl. Phys. Lett.*, **95**, 022111 (2009).
- 3) H. Minemawari, T. Yamada, H. Matsui, J. Tsutsumi, S. Haas, R. Chiba, R. Kumai, and T. Hasegawa, *Nature.*, **475**, 364 (2011).
- 4) R. W. I. de Boer, M. E. Gershenson, A. F. Morpurgo, and V. Podzorov, *Phys. Stat. Sol. A*, **201**, 1302 (2004).
- 5) S. -S. Sun and N. S. Sariciftci: *Organic photovoltaics, Mechanisms, Materials and Devices*, (CRC Press, New York, 2005) chap. 10, p. 239.
- 6) H. Spanggaard, F. C. Krebs, *Sol. Energy Mater. Sol. Cells*, **83**, 125 (2004).
- 7) C. W. Tang, *Appl. Phys. Lett.*, **48**, 183 (1986).
- 8) M. Hiramoto, H. Fujiwara, and M. Yokoyama, *Appl. Phys. Lett.*, **58**, 1062 (1991).
- 9) K. Suemori, Y. Matsumura, M. Yokoyama, and M. Hiramoto, *Jpn. J. Appl. Phys.*, **45**, L472 (2006).
- 10) R.A. Laudise, Ch. Kloc, P. G. Simpkins, T. Siegrist, *J. Cryst. Growth*, **187**, 449 (1998).
- 11) A. Jayaraman, M. L. Kaplan, P. H. Schmidt, *J. Chem. Phys.*, **82**, 4 (1985)
- 12) Built-in field in lateral type cell of $L = 30 \mu\text{m}$ was also evaluated by means of the device simulation. Almost the same value ($4.0 \times 10^2 \text{ V cm}^{-1}$) was obtained.
- 13) R. J. Chesterfield, J. C. McKeen, C. R. Newman, P. C. Ewbank, D. A. Filho, J. L. Bredas, L. L. Miller, K. R. Mann, C. D. Frisbie, *J. Phys. Chem. B*, **108**, 19281 (2004).

Chapter 4:

Lateral Alternating Donor/Acceptor Multilayered Junction for Organic Solar Cells

“Lateral Alternating Donor/Acceptor Multilayered Junction for Organic Solar Cells”

*Mitsuru Kikuchi, Masaki Hirota, Thidarat Kunawong, Yusuke Shinmura, Masahiro Abe, Yuichi Sadamitsu, Aye Myint Moh, Seiichiro Izawa, Masanobu Izaki, Hiroyoshi Naito, and , Masahiro Hiramoto,

ACS Applied Energy Materials, **2**, 2087–2093 (2019).

Abstract

Blended junctions are indispensable for organic solar cells; however, the fabrication of electron and hole transport routes in blended cells remains quite challenging. Herein, a lateral alternating multilayered junction using a high-mobility organic semiconductor is proposed and demonstrated. A total of 93% of the photogenerated electrons and holes are laterally collected over a long distance (0.14 mm). The exciton-collection efficiency reaches 75% in a lateral alternating multilayered junction with a layer thickness of 10 nm. A lateral organic alternating multilayered junction that completely collects both excitons and carriers can be an alternative blended junction for organic solar cells.

4.1. Introduction

Blended junctions are commonly fabricated for modern organic solar cells¹⁻⁸). Conventional organic solar cells are vertically built on indium tin oxide (ITO) glass substrates using a sandwich-type structure⁹⁻¹¹). However, the nanostructure fabrication of the electron and hole transport routes in the blended donor (D) and acceptor (A) molecules based on percolation is still a problem in spite of recent reports on some blended systems where the thickness reached nearly a micron¹²⁻¹⁵). An ideal structure, i.e., a vertical alternating multilayered structure consisting of donor and acceptor molecules that satisfy both exciton collection and carrier collection, has been reported^{16,17}). A vertical alternating multilayered structure is equivalent to the structure shown in **Fig. 4.1a** rotated 90°, and one of the electrode sides acts as a substrate. However, the required aspect ratio reaches 100 because the required distance between adjacent D/A interfaces is less than 10 nm owing to the short exciton diffusion length, and the film thickness required to absorb all incident solar light is 1,000 nm. Thus, the designated fabrication of vertical alternating multilayered structures when using current lithography techniques is still very difficult.

If carrier transport over a long distance parallel to the substrate is possible, the formation of a vertical route is unnecessary. Therefore, we proposed a lateral alternating donor/acceptor multilayered junction (**Fig. 4.1a**). This structure consists of many alternating units of planer heterojunctions between the donor and acceptor layers. An essential point is that the photogenerated holes and electrons are laterally transported and extracted to the respective electrodes. Recently, organic films with high mobilities for holes (reaching $43 \text{ cm}^2 \text{ V}^{-1} \text{ s}^{-1}$)¹⁸⁻²¹) and electrons (reaching $1.7 \text{ cm}^2 \text{ V}^{-1} \text{ s}^{-1}$)²²) were reported. Since high mobility is observed in the direction parallel to the substrate

owing to strong π - π interactions, this is suitable for the proposed device in **Figure 1a**. As a first step, we previously attempted lateral electron collection using an electron-transporting organic single crystal²³). We attempted to fabricate a lateral carrier-collecting multilayered junction (**Fig. 4.1a**). We think that this method is a candidate for fabricating designed nanostructures having abilities similar or superior to blended films by taking account of the rapid progress of high-mobility organic materials having a band conductive nature. We also think that a lateral multilayered junction that is intentionally designed on the nanometer scale can be used to clarify the operation mechanism of blended junctions as well as to replace blended junctions.

Concept: Fig. 4.1a shows the concept of a lateral alternating multilayered junction cell consisting of hole pathways (Fig. 4.1b) and electron pathways (Fig. 4.1c), which are the simplest units. The hole and electron pathways are selectively connected only to the hole- and electron-collecting electrodes by using the respective buffer layers. A photogenerated exciton diffuses to the nearest D/A interface and dissociates. The generated electron and hole move laterally through the electron and hole pathways and are collected by the electron- (right side) and hole-collecting (left side) electrodes, respectively. Exciton collection is achieved through nanometer-scale control of the film thickness. Carrier collection is achieved by long-distance lateral transport of carriers in high-carrier-mobility organic semiconductor films. The present structure can be precisely designed via nanometer-scale control over the film thickness that is independent of the percolation. Moreover, an unlimited vertical thickness is permitted, which allows for the absorption of the entire solar spectrum. In this letter, we demonstrate the operation of a lateral alternating D/A multilayered junction for organic solar cells with a millimeter-scale macroscopic lateral distance between the electrodes.

Carrier pathway unit cells: Hole and electron pathway unit cells are shown in Fig. 4.2a and 4.2d, respectively. In the case of a hole pathway unit cell (Fig. 4.2a), C8-BTBT, which shows a hole mobility (μ_h) of up to $43 \text{ cm}^2 \text{ V}^{-1} \text{ s}^{-1}$ [18,24], was used as the hole transporter. A pair of electrodes separated by distance L was deposited on the film surface. Cells having an L of 0.05, 0.1, 0.2, 0.3, 0.4, 0.5, and 0.6 mm were fabricated. Fullerene (C_{60}), the acceptor (A), was inserted between the C8-BTBT, the donor (D), and the electron-collecting electrode. At the D/A interface, excitons dissociate into electrons and holes under light irradiation. Since the photogenerated electrons move vertically, the distance to the electron-collecting electrode is equal to the

C₆₀ film thickness (50 nm). On the other hand, since the photogenerated holes move in the lateral direction, the distance to the hole-collecting electrode is equal to the interelectrode distance (L), which is longer than 0.05 mm. Since the lateral distance is 1,000 times longer than the vertical distance, the characteristics of the hole pathway unit cells are dominated by the lateral hole transport. The left-hand edge of the electron-collecting electrode can be regarded as the starting line for the holes (solid red line). The range of the holes (L_h) is expressed by Eq. (1) [25–29]:

$$L_h = \mu_h \tau_h E \quad (1)$$

where μ_h , τ_h , and E are the hole drift mobility, the lifetime of holes, and the electric field, respectively. When L is shorter than the range L_h ($L_h > L$) (**Fig. 4.2a**, electrode A), the holes are collected by the hole-collecting electrode. However, when L is longer than the range L_h ($L_h < L$) (**Fig. 4.2a**, electrode C), the holes are not collected. Thus, the magnitude of the photocurrent decreases at approximately $L = L_h$ (**Fig. 4.2a**, electrode B). Conversely, L_h can be determined by observing the sudden drop in the photocurrent. By using the electron pathway unit cells (**Fig. 4.2d**), the electron range (L_e) can be determined in a similar manner. As an electron transporter, PTCDI-C8 (**Fig. 4.2d**), which has a high electron mobility ($\mu_e = 1.7 \text{ cm}^2 \text{ V}^{-1} \text{ s}^{-1}$ [21]), was used. Phthalocyanine (H₂Pc), D, was inserted between the PTCDI-C8, A, and the hole-collecting electrode.

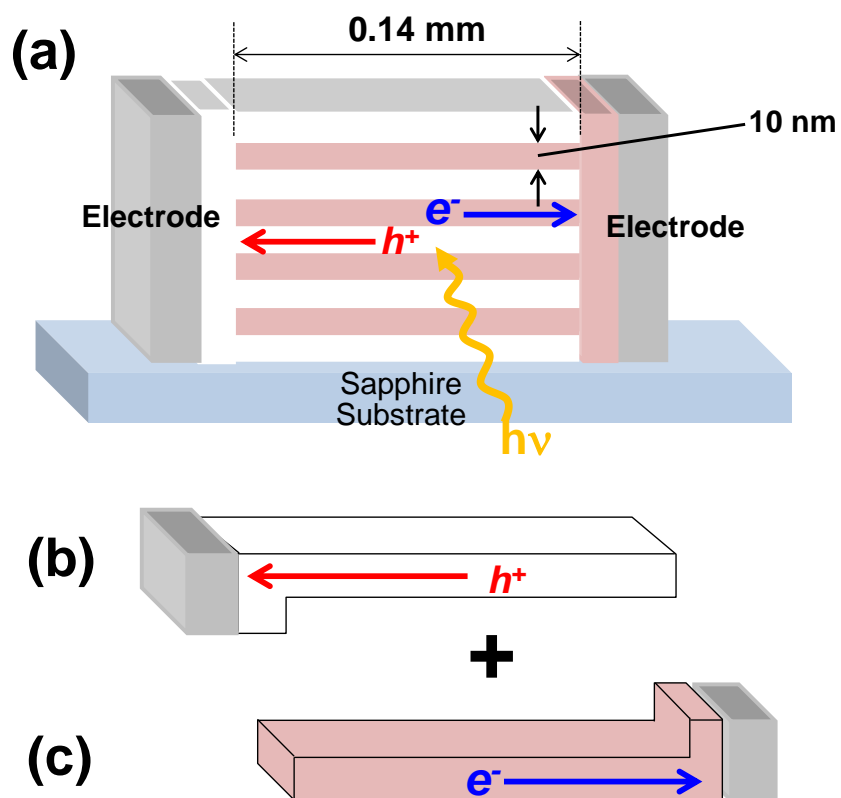


Figure 4.1. (a) Lateral alternating multilayered junction. Present reported junction (Figure 4.5) has layer thickness of 10 nm and lateral distance of 0.14 mm, i.e., aspect ratio reaches 1.4×10^4 . (b) Hole pathway. (c) Electron pathway. (b) and (c) are simplest units for (a).

4.2. Experimental

Materials: C8-BTBT (Nippon Kayaku Co., Ltd.), PTCDI-C8 (Luminescence Technology), MoO₃ (Alfa Aesar), and BCP (bathocuproine) (DOJINDO) were used without purification. C₆₀ (Frontier Carbon Co., Ltd., nanom purple TL) and metal-free phthalocyanine (H₂Pc) (DIC Corporation) were purified by single-crystal sublimation³⁰⁻³². C-plane single-crystal sapphire substrates (Kyocera) which were annealed at 1200°C for 1 h in air (ULVAC, MILA5000) were used.

Vacuum deposition: Organic semiconductors were deposited under a pressure of 10⁻⁶ Pa at room temperature in an oil-free vacuum chamber housed in a glove box (EpiTech Inc., 12ET12007). The evaporation rate of C8-BTBT, PTCDI-C8, C₆₀, and H₂Pc was 0.1 nm s⁻¹.

Fabrication of hole pathway cell (Fig. 4.2a): C8-BTBT (50 nm) was deposited on C-sapphire substrates since C8-BTBT films with high crystallinities grown by vacuum deposition have been reported³³. The c-axis of the C8-BTBT molecules was confirmed to be oriented perpendicular to the substrate by X-ray diffraction. Metal masks with two square apertures separated from each other by the desired distance L (0.05, 0.1, 0.2, 0.3, 0.4, 0.5, and 0.6 mm) were used to form the electrode pairs. C₆₀ (50 nm) and an electron-collecting electrode (BCP/Ag) were deposited on the C8-BTBT film through one of the apertures. Then, a hole-collecting electrode (MoO₃/Ag) was deposited through another aperture.

Fabrication of electron pathway cell (Fig. 4.2d): PTCDI-C8 (50 nm) was deposited on the C-sapphire substrates. The c-axis of the PTCDI-C8 molecules was confirmed to be oriented perpendicular to the substrate by X-ray diffraction. Metal masks with two square apertures separated from each other by the desired distance L (0.05, 0.1, 0.2,

0.3, and 0.4 mm) were used to form the electrode pairs. H₂Pc (50 nm) and a hole-collecting electrode (MoO₃/Ag) were deposited on the PTCDI-C8 film through one of the apertures. Then, an electron-collecting electrode (BCP/Ag) was deposited through another aperture.

Fabrication of lateral multilayered junction (Fig. 4.1a, Figure 2.8 (in chap. 2)): C8-BTBT, acting as the hole pathway, and PTCDI-C8, acting as the electron pathway, were vacuum deposited alternately on sapphire substrate. Each layer thickness of the C8-BTBT and PTCDI-C8 films was decreased from 50 to 25 to 10 nm while keeping the thickness of the C8-BTBT and PTCDI-C8 films the same. The total thickness of the multilayered junction was maintained at 100 nm. The C8-BTBT and PTCDI-C8 films were selectively connected to only the hole- and electron-collecting electrodes, respectively, by using a customized movable mask system (EpiTech, Inc.) (**Figure 2.8 (in chap. 2)**).

Measurements: The current-voltage (J-V) characteristics were measured under simulated solar light irradiation (ASAHI Spectra, HAL-320) from the substrate side in a vacuum. The photocurrent action spectra were measured under irradiation by monochromatic light using a monochromator (Shimadzu, SPG-100ST). The number of incident photons was determined by the same measurement using a standard silicon diode (Hamamatsu Photonics, S1337-66BQ). None of the cells were exposed to air at any time during fabrication or testing.

4.3. Results and Discussion

4.3.1 Carrier ranges

Fig. 4.2c shows the current-voltage (J-V) characteristics of the hole-transporting cells. At $L = 0.05$ mm, a clear photovoltaic curve was observed (red curve). Photovoltaic effects were observed for L values of 0.05, 0.1, 0.2, 0.3, 0.4, 0.5, and 0.6 mm. A sudden decrease in the photocurrent was observed between $L = 0.4$ and 0.5 mm, and the photocurrent disappeared at $L = 0.6$ mm.

The dependences of the photocurrent for constant electric field strengths (E) between the lateral electrodes of 0 (black), -10 (red), -20 (green), and -30 V cm^{-1} (blue), which were calculated by dividing the reverse applied voltage by L , on the electrode distance (L) are shown in **Fig. 4.2b**. Here, $E = 0 \text{ V cm}^{-1}$ corresponds to the short-circuit condition. Sudden drops in the photocurrent at $L = 0.4$ mm were observed for all E values. Thus, we concluded that the hole range (L_h) is 0.4 mm. When a typical hole-transporting material [NPD; N,N-di(1-naphthyl)-N,N-diphenyl-(1,1-biphenyl)-4,4-diamine] with a low mobility of $\mu_h = 1.0 \times 10^{-4} \text{ cm}^2 \text{ V}^{-1} \text{ s}^{-1}$ was used, no photocurrent was observed, even at $L = 50 \text{ }\mu\text{m}$ (**Fig. 4.3**). Obviously, the high mobility of C8-BTBT is responsible for the long hole range (L_h) reaching 0.4 mm (**Fig. 4.4**).

The cross-section area of the C8-BTBT film is $1 \times 10^{-6} \text{ cm}^2$ since the film thickness and width are 50 nm and 2 mm, respectively (**Fig. 4.2b**, black broken rectangle). Thus, the cross-sectional current density through the hole-transporting layer reached 0.75 A cm^{-2} with a very low electric field (-30 V cm^{-1}) (see the right vertical axis in **Fig. 4.2b**). Obviously, the C8-BTBT film acts as an excellent lateral hole pathway.

The electron pathway unit cells showed clear photovoltaic curves. Sudden drops in the photocurrent for $L = 0.2$ mm were observed at $E = 0, -10, -20,$ and -30 V cm^{-1} (Figure 2.1e). Thus, the electron range (L_e) was determined to be 0.2 mm. Moreover, the cross-sectional current density through the electron-transporting layer reached 10 mA cm^{-2} with a very low electric field (30 V cm^{-1} , see the right vertical axis in Figure 2.1e). Obviously, the PTCDI-C8 film acts as an excellent lateral electron pathway.

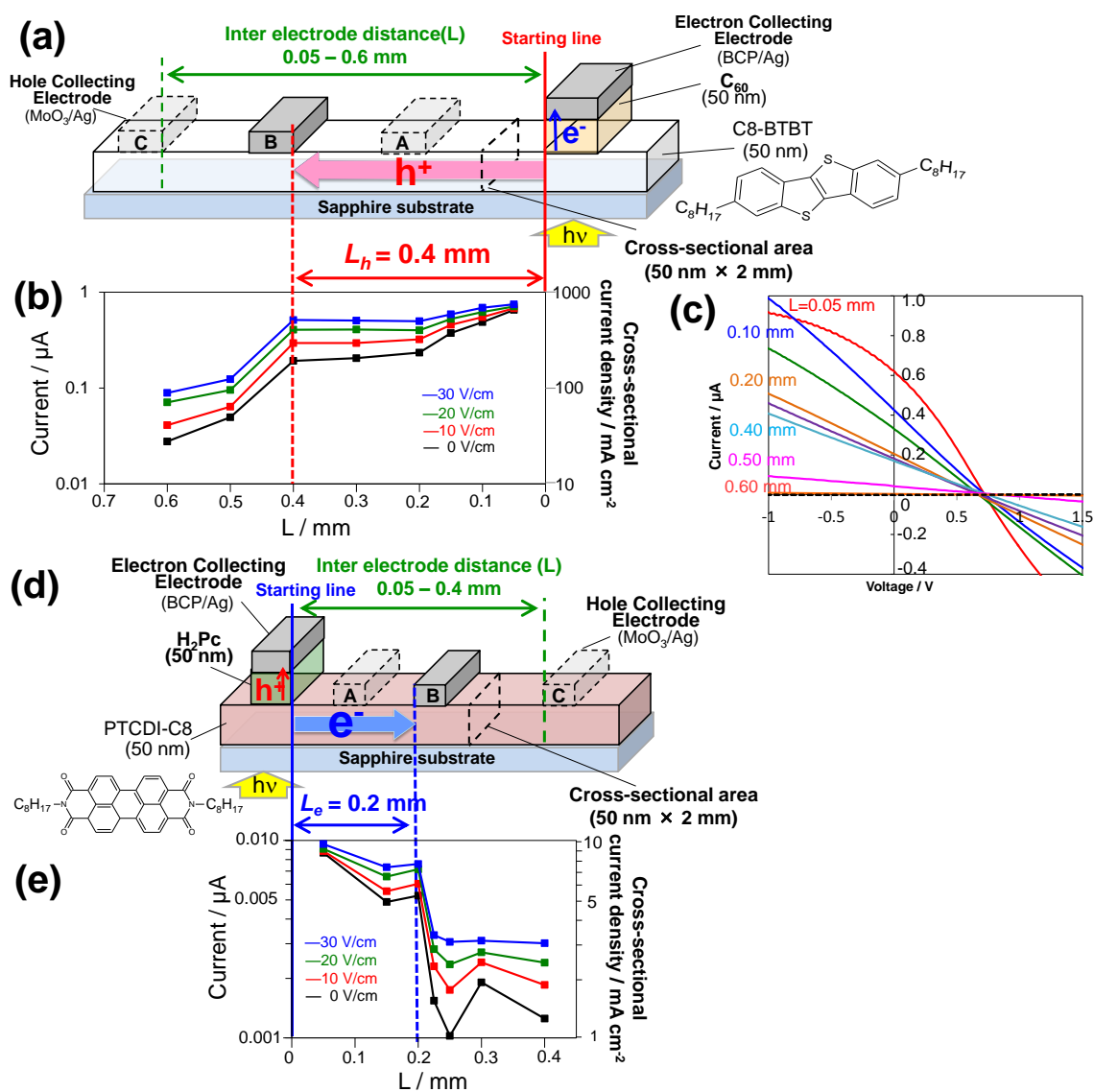


Figure 4.2. (a) Hole pathway unit cells having electrode distance (L) from 0.05 to 0.6 mm. (b) Dependences of photocurrent magnitude on L under constant electric fields of 0 (black), 10 (red), 20 (green), and 30 V cm^{-1} (blue) between lateral electrodes. Current density calculated from area of cross section of C8-BTBT film is shown on right vertical axis. (c) Current-voltage (J - V) characteristics of hole pathway unit cells. (d) Electron pathway unit cells having L from 0.05 to 0.4 mm. (e) Dependence of photocurrent magnitude on L under constant electric field strengths of 0 (black), 10 (red), 20 (green), and 30 V cm^{-1} (blue).

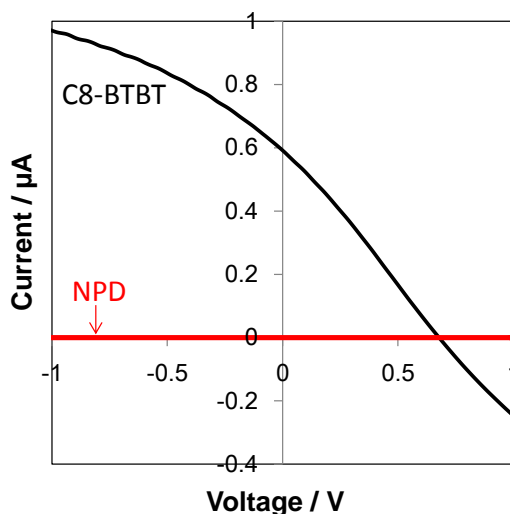


Figure 4.3. Current-voltage (J - V) characteristics of cells shown in **Fig. 4.1b** with $L = 50$ μm using C8-BTBT film (black curve) and NPD film (red curve). NPD cell shows no J_{SC} and no V_{OC} .

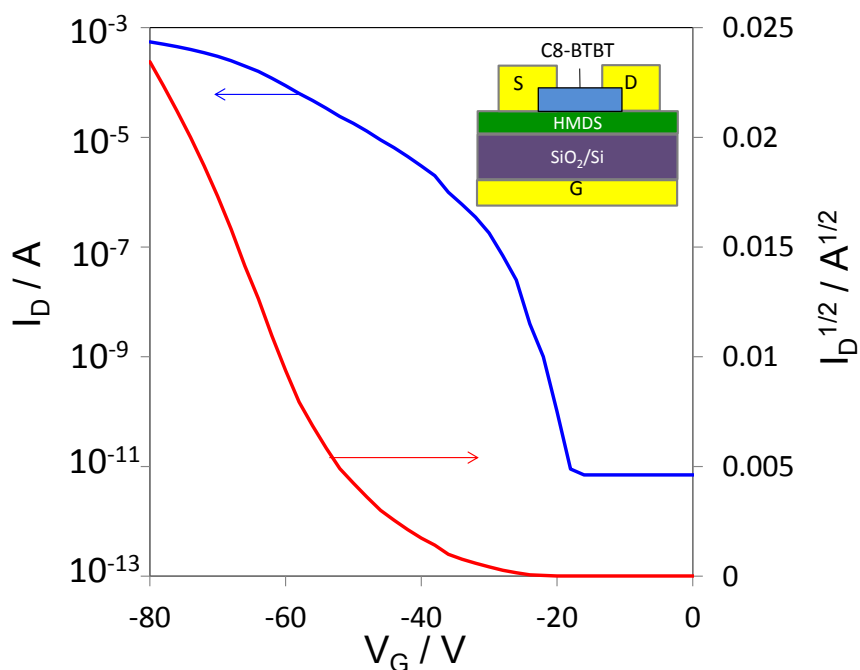


Figure 4.4. Transfer characteristics (I_D - V_G) of field effect transistor (FET) device using vacuum deposited C8-BTBT film (50 nm). FET structure is shown as inset. Channel length and width are 50 μm and 2 mm, respectively. As a gate electrode, SiO_2/Si treated with hexamethyldisilazane (HMDS) was used. Drift mobility (μ_h) of $2.3 \text{ cm}^2 \text{ V}^{-1} \text{ s}^{-1}$ was obtained. Lifetime of holes (τ_h) at $E = 30 \text{ V cm}^{-1}$ (**Fig. 4.2b**, blue) was calculated at 0.6 ms for hole range (L_h) of 0.4 mm and drift mobility (μ_h) of $2.3 \text{ cm}^2 \text{ V}^{-1} \text{ s}^{-1}$. Long hole range (L_h) reaching 0.4 mm can be attributed to high mobility (μ_h) and significantly long lifetime of holes (τ_h). It should be noted that, strictly speaking, even though at $E = 0 \text{ Vcm}^{-1}$ corresponding to short-circuit condition, there is a potential gradient in cell consisting of built-in-potential in D/A interface and voltage drop across C8-BTBT film.

4.3.2 Lateral Alternating Multilayered Junction

The hole range ($L_h = 0.4$ mm) and the electron range ($L_e = 0.2$ mm) were determined. Thus, we adjusted the width of the overlap between C8-BTBT and PTCDI-C8 in the lateral alternating multilayered junction to less than 0.4 mm and 0.2 mm, i.e., 0.14 mm for the total extractions of holes and electrons to the respective electrode (**Fig. 4.1a**). The hole and electron pathways were selectively connected to only the hole- and electron-collecting electrodes, respectively (**Fig. 4.1a**) by using a custom-made movable masking system (**Fig. 2.8 (in chap. 2)**). The total number of pathway layers increased, while the total thickness of the alternating multilayered junction was maintained at 100 nm.

Superior photovoltaic characteristics were observed (**Fig. 4.5a**). An open-circuit voltage (V_{OC}) between 0.88 and 1.0 V and a fill factor (FF) between 0.36 and 0.48 were observed, which is surprising considering the small electric fields at short-circuit condition (70 V cm^{-1}) and even smaller electric field near the open-circuit condition ($\ll 70 \text{ V cm}^{-1}$) (**Fig. 4.5a**). The photocurrent density was proportional to the simulated solar light intensity between 25 and 500 mW cm^{-2} (**Fig. 4.5b**). The photocurrent density per cross-sectional area of the multilayered film reached 0.4 A cm^{-2} (**Fig. 4.5b**, right vertical axis). Thus, the photovoltaic operation of lateral alternating multilayered junctions with a macroscopic lateral electrode distance of 0.14 mm was demonstrated.

A corresponding vertical cell with an ITO/MoO₃/C8-BTBT(50 nm)/PTCDI-C8(50 nm)/BCP/Ag structure is usually operated with a built-in electric field under short-circuit conditions that are 10^4 -times larger (10^5 V cm^{-1}) when a cell thickness of 100 nm and V_{OC} of 1 V are considered.

By increasing the number of layers from 2 (black curve) to 4 (blue curve) to 10 (red curve), i.e., by decreasing the D/A interface distance from 50 to 25 to 10 nm, a dramatic increase in the photocurrent was observed. Photogenerated excitons within a diffusion length of the exciton from the D/A interface can reach the D/A interface (active layer) (**Fig. 4.5e**, red region). However, excitons photogenerated at distances greater than the exciton diffusion length cannot reach the D/A interface (dead layer) (**Fig. 4.5e**, pink region). Gradual elimination of the dead layer by decreasing the D/A interface distance (**Fig. 4.5e**, from left to right) increases the exciton-collection efficiency (η_{EC}). Thus, a dramatic increase in the photocurrent occurs.

The action spectra of the internal quantum efficiency (IQE) and the external quantum efficiency (EQE) of the short-circuit photocurrent (J_{SC}) for these cells are shown in **Fig. 4.5c** and **Fig. 4.6**, respectively. By increasing the number of layers from 2 to 4 to 10, i.e., by decreasing the D/A interface distance, dramatic increases in the IQE were observed. The exciton-collection efficiency (η_{EC}) can be quantitatively evaluated by using the IQE. The photocurrent owing to irradiation with visible wavelengths (400–600 nm) is generated by PTCDI-C8 since C8-BTBT is transparent. The semilogarithmic plots of the IQE at various wavelengths vs. the PTCDI-C8 thickness are linear (**Fig. 4.5d**). The slope of the plot gives an exciton diffusion length of 12 nm, which is the distance at which 50% of the excitons can reach the D/A interface. By assuming that η_{EC} is 100% at 0 nm, η_{EC} for five monolayers of PTCDI-C8 with a thickness of 10 nm was 75% (**Fig. 4.5e**, right enlarged illustration). Thus, we concluded that the lateral alternating multilayered junction can collect most of the photogenerated excitons at the D/A interfaces.

The clear saturation behavior of photocurrent that is independent of the reverse bias (**Fig. 4.5a**) strongly suggests that most of the photogenerated electrons and holes are extracted laterally. Moreover, the proportional relationship between photocurrent and light intensity (**Fig. 4.5b**) suggests that the carrier recombination during lateral carrier transport is negligible. Thus, we concluded that the carrier-collection efficiency (η_{CC}) in the region of photocurrent saturation is unity. Therefore, η_{CC} of 93%, which is determined by the ratio of the J_{SC} value to the photocurrent in the saturated region, was obtained (**Fig. 4.5a**, red curve).

With the present D/A combination of C8-BTBT and PTCDI-C8, the exciton dissociation efficiency (η_{ED}) was very small and was calculated to be 0.3% using Eq. (2).

$$IQE = \eta_{EC}\eta_{ED}\eta_{CC} \quad (2)$$

We presume that this low efficiency is owing to the long alkyl chains of C8-BTBT and PTCDI-C8 acting as 2-nm-thick insulators and inhibiting the initial charge separation. However, the lateral alternating multilayered junction (**Fig. 4.5a**) is a universal principle, and various kinds of organic semiconductors are suitable for use in lateral alternating multilayered junctions. One of the advantages of a lateral carrier-collecting alternating multilayered cell is its unlimited thickness in the vertical direction. Therefore, tandem solar cells that can utilize the full solar spectrum can be freely designed. Owing to the millimeter-scale macroscopic lateral distance between the electrodes, modules with large surface areas can be fabricated by a simple masking system.

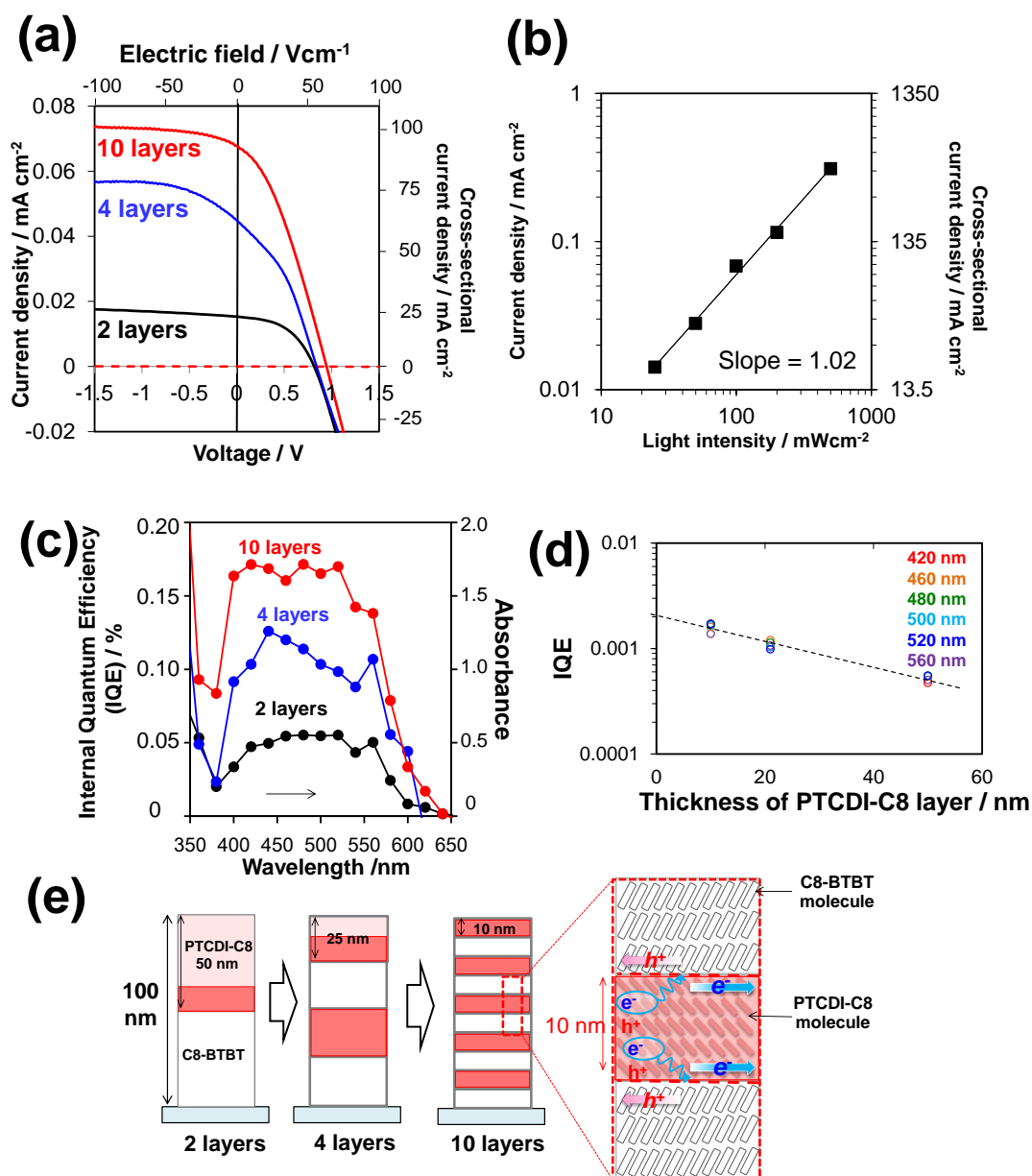


Figure 4.5. (a) Current-voltage (J - V) characteristics of lateral alternating multilayered junctions of 2-layered (black), 4-layered (blue), and 10-layered (red) devices. Photocurrent density per cell area is shown on left vertical axis. Effective electric field in cell is shown on upper horizontal axis. Photocurrent density per cross-sectional area of multilayered film is shown on right vertical axis. Broken curve is dark current. (b) Dependence of short-circuit photocurrent density (J_{SC}) on simulated solar light intensity between 0.25 and 5 suns (from 25 to 500 mW cm^{-2}) for 10-layered alternating

multilayered cell. (c) Action spectra of internal quantum efficiency (IQE) of J_{SC} for each number of layers. Absorption spectrum of film having total thickness of C8-BTBT (50 nm) and PTCDI-C8 (50 nm) is also shown (black curve). (d) Semilogarithmic plots of dependence of IQE at various wavelengths on PTCDI-C8 layer thickness. (e) Active region (red) and dead region (pink) of exciton collection in 2-, 4-, and 10-layered cells. Layer thickness of 10 nm corresponds to 5 and 3 molecules of PTCDI-C8 and C8-BTBT, respectively.

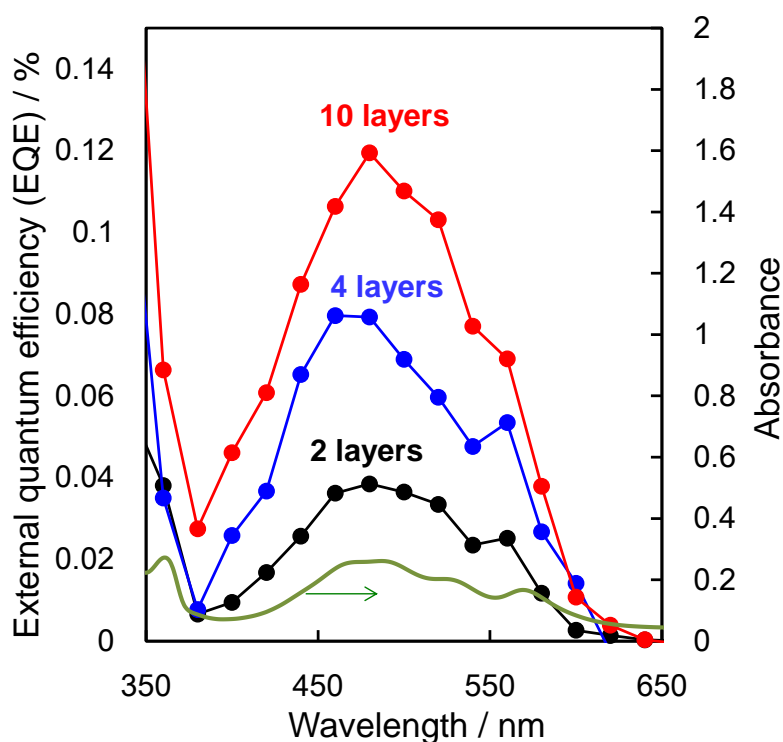


Figure 4.6. (a) Action spectra of external quantum efficiency (EQE) of short-circuit photocurrent (J_{SC}) for each number of layers. Absorbance of film having total thickness of C8-BTBT (50 nm) and PTCDI-C8 (50 nm) is also shown.

4.4. Conclusion

In conclusion, the lateral organic alternating multilayered junction has an ability to collect both excitons and carriers almost completely. A lateral alternating multilayered junction can be regarded as an alternative blended junction for organic solar cells.

4.5. References

- 1) M. Hiramoto, H. Fujiwara, M. Yokoyama, *Appl. Phys. Lett.*, **58**, 1062 (1991).
- 2) G. Yu, J. Gao, J.C. Hummelen, F. Wudl, A.J. Heeger, *Science*, **270**, 1789 (1995).
- 3) B. Maennig, J. Drechsel, D. Gebeyehu, P. Simon, F. Kozlowski, A. Werner, F. Li, S. Grundmann, S. Sonntag, M. Koch, K. Leo, M. Pfeiffer, H. Hoppe, D. Meissner, N.S. Sariciftci, I. Riedel, V. Dyakonov, J. Parisi, *Appl. Phys. A*, **79**, 1 (2004).
- 4) M. Riede, C. Uhrich, J. Widmer, R. Timmreck, D. Wynands, G. Schwartz, W.M. Gnehr, D. Hildebrandt, A. Weiss, J. Hwang, S. Sundarraj, P. Erk, M. Pfeiffer, K. Leo, *Adv. Funct. Mater.* **21**, 3019–3028(2011).
- 5) W.N. Li, L. Ye, S. S. Li, H. F. Yao, H. Ade, J. H. Hou, *Adv. Mater.* 1707170 (2018).
- 6) I. Osaka, M. Saito, T. Koganezawa, K. Takimiya, *Adv. Mater.*, **26**, 331 (2014).
- 7) T. Kaji, M. Zhang, S. Nakao, K. Iketaki, K. Yokoyama, C. W. Tang, M. Hiramoto, *Adv. Mater.*, **23**, 3320 (2011).
- 8) S. -S. Sun, N. S. Sariciftci, *Organic photovoltaics, Mechanisms, Materials and Devices*, (CRC Press, New York, 2005) chap. 10, p. 239.
- 9) H. Spanggaard, F. C. Krebs, *Sol. Energy Mater. Sol. Cells*, **83**, 125 (2004).
- 10) C. W. Tang, *Appl. Phys. Lett.*, **48**, 183 (1986).
- 11) K. Walzer, B. Maennig, M. Pfeiffer, K. Leo, *Chem. Rev.* **107**, 1233 (2007).
- 12) I. Osaka, M. Saito, T. Koganezawa, K. Takimiya, *Adv. Mater.* **26** 331–338 (2014).
- 13) K. Sakai, M. Hiramoto, *Mol. Cryst. Liq. Cryst.*, **491**, 284–289 (2008).
- 14) A. Armin, J. Subbiah, M. Stolterfoht, S. Shoaee, Z. Xiao, S. Lu, D. J. Jones, P. Meredith, *Adv. Energy Mater.*, **6**, 1600939, (2016).

- 15) Y. Jin, Z. Chen, S. Dong, N. Zheng, L. Ying, X.F. Jiang, F. Liu, F. Huang, Y. Cao, *Adv. Mater.* **28**, 9811–9818(2016).
- 16) M. Hiramoto, T. Yamaga, M. Danno, K. Suemori, Y. Matsumura, M. Yokoyama, *Appl. Phys. Lett.* **88**, 213105 (2006).
- 17) Y. Matsuo, Y. Sato, T. Niinomi, I. Soga, H. Tanaka, E. Nakamura, *J. Am. Chem. Soc.*, **131**, 16048 (2009).
- 18) Y. Yuan, G. Giri, A. L. Ayzner, A. P. Zoombelt, S. C. B. Mannsfeld, J. Chen, D. Nordlund, M. F. Toney, J. Huang Z. Bao., *Nat. Commun.*, **5**, 3005 (2014).
- 19) J. Takeya, M. Yamagishi, Y. Tominari, R. Hirahara, Y. Nakazawa, *Appl. Phys. Lett.*, **90**, 1021120 (2007).
- 20) H. Minemawari, T. Yamada, H. Matsui, J. Tsutsumi, S. Haas, R. Chiba, R. Kumai, T. Hasegawa, *Nature*, **475**, 364 (2011).
- 21) S. Haas, Y. Takahashi, K. Takimiya, T. Hasegawa, *Appl. Phys. Lett.*, **95**, 022111 (2009).
- 22) R. J. Chesterfield, J. C. McKeen, C. R. Newman, P. C. Ewbank, D. A. S. Filho, J.-L. Brédas, L. L. Miller, K. R. Mann, C. D. Frisbie. *J. Phys. Chem. B*, **108**, 19281-19292 (2004).
- 23) M. Kikuchi, K. Takagi, H. Naito, M. Hiramoto, *Org. Electron.*, **41**, 118-121 (2017).
- 24) K. Takimiya, S. Shinamura, I. Osaka, E. Miyazaki, *Adv. Mater.*, **23**, 4347 (2011).
- 25) H. Naito, Y. Kanemitsu, *Phys. Rev. B* , **49**, 49 (1994).
- 26) V. Coropceanu, J. Cornil, D. A. da Silva Filho, Y. Olivier, R. Silbey, and J.-L. Bredas, *Chem. Rev.*, **107**, 926-952 (2007).
- 27) P. G. Lecomber, W. E. Spear, *Phys. Rev. Lett.*, **25**, 509 (1970).

- 28) F. W. Schmidlin, *Phys. Rev. B*, **16**, 2362 (1977).
- 29) V. Podzorov, E. Menard, A. Borissov, V. Kiryukhin, J. A. Rogers, M. E. Gershenson, *Phys. Rev. Lett.* **93**, 1 (2004).
- 30) R.A. Laudise, C. Kloc, P. G. Simpkins, T. Siegrist, *J. Cryst. Growth*, **187**, 449 (1998).
- 31) K. Sakai, M. Hiramoto, *Mol. Cryst. Liq. Cryst.*, **491**, 284 (2008).
- 32) M. Hiramoto, M. Kubo, Y. Shinmura, N. Ishiyama, T. Kaji, K. Sakai, T. Ohno, M. Izaki, **3**, 351 (2014).
- 33) A. M. Moh, P. L. Khoo, K. Sasaki, S. Watase, T. Shinagawa, M. Izaki, *Phys. Status Solidi A*, 1700862 (2018).

Chapter 5:

Doped Organic Single-Crystal Photovoltaic Cells

“Doped Organic Single-Crystal Photovoltaic Cells”

*Mitsuru Kikuchi, Sureerat Makmuang, Seiichiro Izawa, Kanet Wongravee, Masahiro Hiramoto,
Org. Electron., **64**, 92-96 (2019).

Abstract

Doped rubrene single-crystal photovoltaic cells were fabricated. Whole photocurrent generated in the *pn*-homojunction with the macroscopic area of 2 mm × 1 mm was confirmed to be collected through the *p*-doped homoepitaxial layer. A single-crystal substrate collected excitons to the *pn*-homojunction with the collection efficiency reaching 46%, owing to the long exciton diffusion length of 2.7 μm.

5.1. Introduction

Recently, organic single-crystal devices have been the subject of significant research interest.¹⁻⁵⁾ Organic single crystals with high carrier mobility, reaching $40 \text{ cm}^2\text{V}^{-1}\text{s}^{-1}$,⁶⁻⁹⁾ have been reported. Because high carrier mobility is manifested parallel to the crystal surface along the π - π stacking of organic molecules, lateral-type organic single-crystal cells have been reported.¹⁰⁾ On the other hand, a long diffusion length of excitons in organic single crystals such as anthracene has been suggested earlier.¹¹⁻¹³⁾ Recently, a long exciton diffusion length (2–8 μm) was reported for rubrene single crystals.¹⁴⁾ Although these findings strongly suggest the suitability of organic single crystals to photovoltaic cells, there remains a hurdle related to the carrier collection, which stems from the high resistivity of these crystals owing to the absence of free carriers. Recently, we developed a bulk-doping technique for homoepitaxially grown rubrene single-crystal layers.¹⁵⁾ This technique can offer a doped high-conductivity route in organic single crystals for carrier collection. Thus, in this study, we tried to fabricate doped rubrene single-crystal photovoltaic cells.

A doped organic single-crystal cell is schematically shown in Fig. 5.1. A *p*-doped single crystalline layer, homoepitaxially grown on a single crystal, acts as a *p*-type hole-transporting layer (Fig. 5.1, blue rectangular part). A *pn*-homojunction, directly connected to an electron-collecting electrode (Fig. 5.1, red rectangular part), is formed on this *p*-type hole-transporting layer. Under the light irradiation, excitons that are generated in an undoped crystal substrate (Fig. 5.1, orange rectangular part) diffuse to the *pn*-homojunction, yielding an intrinsic electric field, and dissociate. Holes that are generated in the *pn*-homojunction are collected by a hole-collecting electrode

through a *p*-type hole-collecting route. Electrons that are generated in the *pn*-homojunction are directly collected by the electron-collecting electrode.

The doped organic single crystal cell (Fig. 5.1) is a function-separated photovoltaic cell. The *p*-type homoepitaxial layer (blue rectangular part) acts as the hole transporter. The *pn*-homojunction (red rectangular part) acts as the exciton dissociator. The single crystal substrate (orange rectangular part) acts as the exciton collector. The internal quantum efficiency (IQE) of the photocurrent is given by equation (1).

$$\text{IQE} = \eta_{EC} \eta_{ED} \eta_{CC} \quad (1).$$

Here, η_{EC} , η_{ED} , and η_{CC} represent the exciton collection efficiency, the exciton dissociation efficiency, and the carrier collection efficiency, respectively.

In this paper, we report the photovoltaic operation of the doped rubrene single-crystal cell.

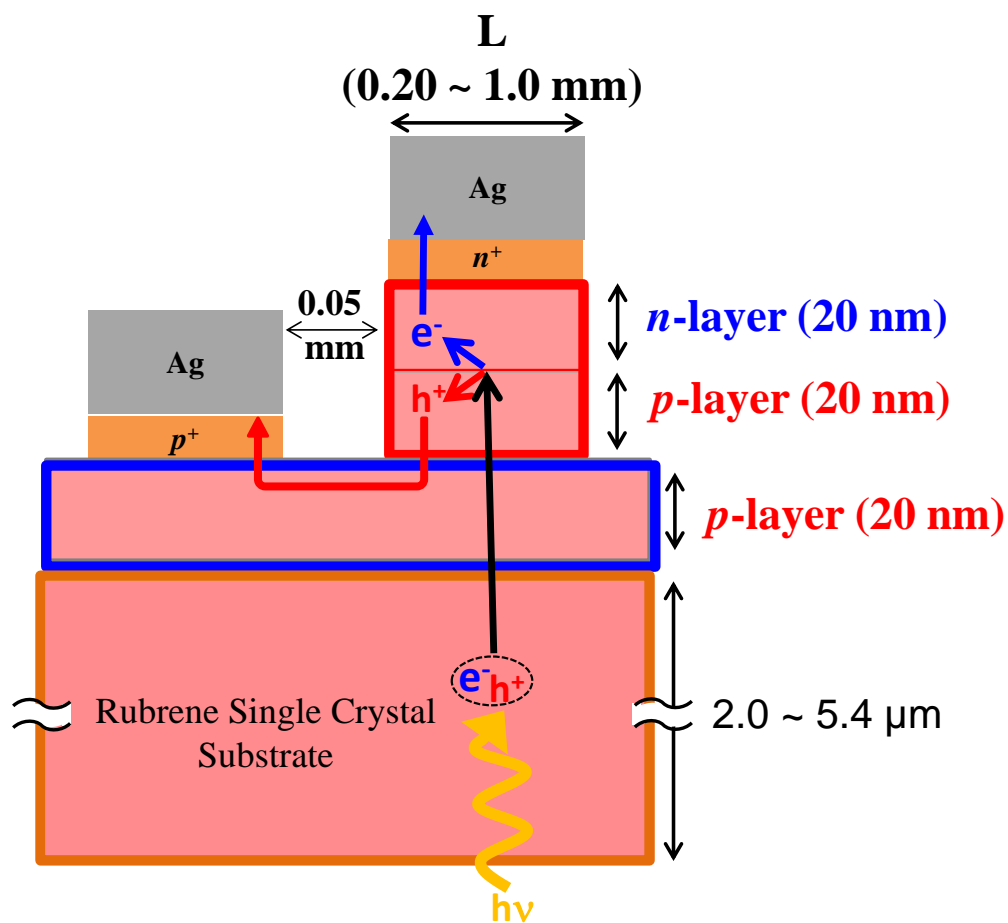


Fig. 5.1 Structure of the fabricated doped organic single-crystal photovoltaic cell.

5.2. Experimental

Single crystals of rubrene (Tokyo Chemical Industry) were grown by physical vapor transport in N₂ (0.1 atm).^{16,17)} The thicknesses of the crystals were in the 2–5.4 μm range. Homoepitaxial films of rubrene were grown on the rubrene single-crystal substrate by depositing at a low evaporation rate of 3.3×10^{-3} nm s⁻¹ at room temperature,^{15,18)} using a vacuum evaporator housed in a glove box (EpiTech Inc., 12ET12007). Doping was performed by co-evaporation. Fe₂Cl₆ (Sigma-Aldrich, 99.99%)^{19,20)} and Cs₂CO₃ (Sigma-Aldrich, 99.999%)^{21,22)} were used for the acceptor and donor dopants, respectively. The doping concentrations of 10 and 100 ppm in volume correspond to the dopant evaporation rates of 3.3×10^{-8} and 3.3×10^{-7} nm s⁻¹, which were realized by reducing the evaporation rate using rotating disks with slits with the aperture ratio of 1:100. The *p*⁺- and *n*⁺-rubrene films (thickness, 10 nm) that were heavily doped with Fe₂Cl₆ and Cs₂CO₃ at the concentration of 10,000 ppm were inserted between the Ag electrodes and *p*- and *n*-type crystals, to form ohmic contacts (Fig. 1). The lateral gap between the two electrodes was kept at 0.05 mm. The width of the *pn*-homojunction, i.e., that of the Ag electrodes, was kept at 2 mm. The area of the *pn*-homojunction (Fig. 5.1, red part) was 2 mm × *L* mm. Here, *L* represents the length of the *pn*-homojunction (Fig. 5.1). The value of *L* was varied from 0.2 to 1.0 mm. On the other hand, hole-only devices²³⁾ with two ohmic electrodes (*p*⁺-layer/Au) in contact with the *p*-layer (Fig. 5.2(a), insets) were fabricated for evaluating the characteristics of the *p*-layer (Fig. 5.1, blue rectangular part).

Current – voltage (*J–V*) characteristics were measured under irradiation by simulated solar light with the light intensity ranging from 0.05 to 10 suns (Asahi Spectra, HAL-320). The photocurrent action spectra were measured under the irradiation by

monochromatic light using a monochromator (Shimadzu, SPG-100ST). Hall measurements were performed for hole-only devices (Fig. 5.2(a), insets) with the van der Pauw four-electrode system using a Hall effect measurement system (Toyo Corp., ResiTest 8300). During the fabrication of cells and during measurements the analyzed samples were not exposed to air.

5.3. Results and Discussion

5.3.1 The characteristics of *p*-type homoepitaxial layer

To evaluate the characteristics of the *p*-layer (Fig. 5.1, blue rectangular part), hole-only devices with the *p*-type homoepitaxial rubrene layer doped with Fe₂Cl₆ (100 ppm) (Fig. 5.2(a), insets) were fabricated. Fig. 5.2(a) shows the dependence of the hole concentration per area ($N_{\square}/\text{cm}^{-2}$) (red dots) on the *p*-layer's thickness, evaluated using the Hall effect measurements. N_{\square} increased proportionally to the *p*-layer's thickness. Obviously, the number of holes increased proportionally to the *p*-layer's thickness. Thus, we obtained the hole concentration per unit volume (N/cm^{-3}) (blue dots) of $2.6 \times 10^{17} \text{ cm}^{-3}$, which was independent of the *p*-layer's thickness. This clearly proves that the holes that are responsible for the carrier transport in these crystals are generated in the *p*-layer. Fig. 5.2(b) shows the dependence of the hole mobility (μ_H) and the specific conductivity (σ) on the *p*-layer's thickness. Though the slight decrease of μ_H causing the slight decrease of σ was observed, the *p*-layer has the significant high value of μ_H of $1.5 \text{ cm}^2 \text{ V}^{-1} \text{ s}^{-1}$ (20 nm).

Fig. 5.2(c) shows the dark current-voltage (*J-V*) characteristics of a hole-only device with a 20-nm-thick *p*-layer. Ohmic behavior was observed (Fig. 5.2(c)). Thus, we concluded that ohmic contacts to *p*-type rubrene single crystal are formed by using the p^+/Ag electrode.²⁴⁾ Current density reached 5250 mA cm^{-2} at 4 V (right vertical axis) and the specific conductivity (σ) of $5.4 \times 10^{-2} \text{ S cm}^{-1}$ was obtained under the condition of the current flowing through the *p*-layer with the cross-sectional area of $20 \text{ nm} \times 2 \text{ mm}$. The value of the specific conductivity ($5.4 \times 10^{-2} \text{ S cm}^{-1}$) agreed well with that measured using the van der Pauw configuration ($6.0 \times 10^{-2} \text{ S cm}^{-1}$). Thus, we concluded that the *p*-type homoepitaxial layer (Fig. 5.1, blue rectangular part) can act as

a lateral hole transporter.

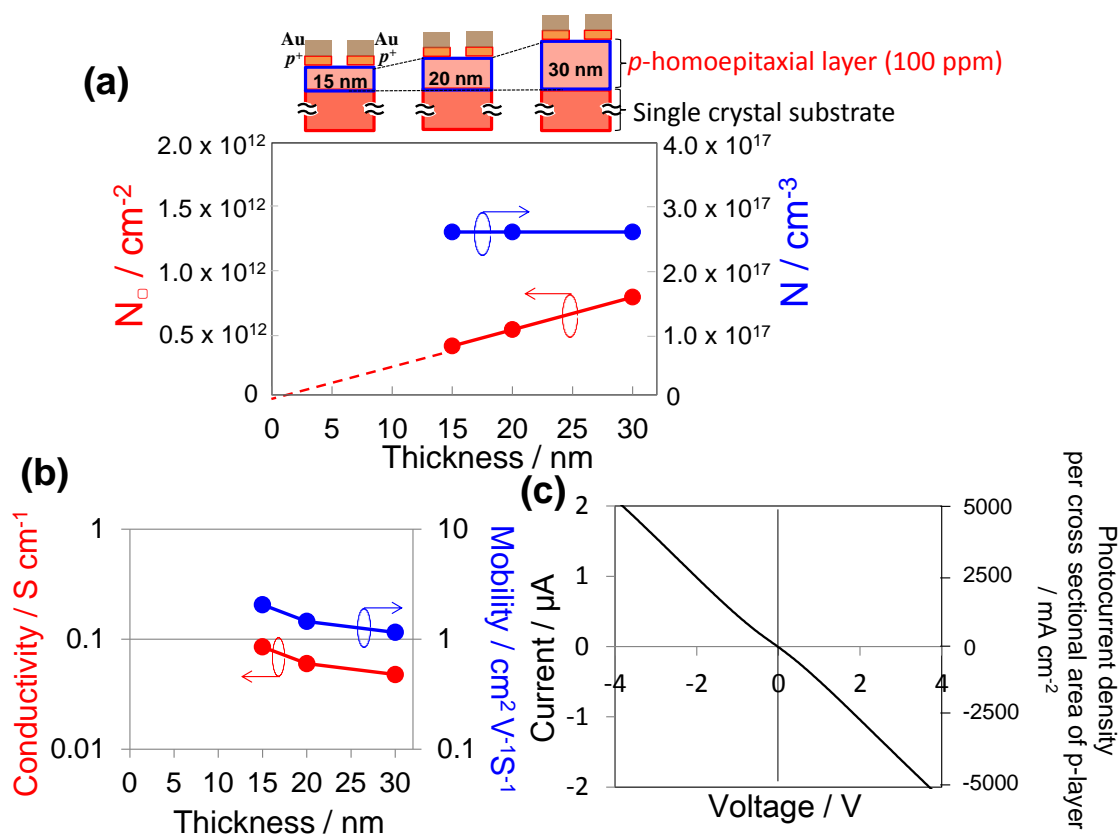


Fig. 5.2 (a) Dependence of the hole concentration per area (N_D) (left vertical axis) (red dots) and of the hole concentration per unit volume (N) (right vertical axis) (blue dots) on the p -layer's thickness. The structures of hole-only devices are also shown (insets). (b) Dependence of the hole mobility (μ_H) and the specific conductivity (σ) on the p -layer's thickness. (c) Dark current-voltage (J - V) characteristics for a hole-only device with the 20-nm-thick p -layer. The right vertical axis shows the current density per the cross-sectional area of the p -layer.

5.3.2 Doped organic single-crystal photovoltaic cells

Fig. 5.3(a) shows the J - V characteristics of doped organic single-crystal photovoltaic cells with both the p -layer (Fig. 5.1, blue part) and the pn -homojunction (Fig. 5.1, red part) (Fig. 5.3(a), red curves), only the p -layer (Fig. 5.1, blue part) (Fig. 5.3(a), black curve), and only the pn -homojunction (Fig. 5.1, red part) (Fig. 5.3(a), blue curves). A clear photovoltaic effect was observed in the cell with both the p -layer and the pn -homojunction (red curve). However, the photovoltaic effect was not observed in the cells without the p -layer (blue curve) or without the pn -homojunction (black curve). Therefore, we concluded that the photovoltaic effect in the analyzed organic single crystals appeared only when both the conditions of the lateral hole transport by the p -layer and the photocarrier generation in the pn -homojunction were satisfied.

The photocurrent density per the cross-sectional area of the p -layer in the short-circuit condition (Fig. 5.3(a), right vertical axis) for the cell (Fig. 5.3(a), red curve, w/ pn junction, w/ p -layer) was 120 mA cm^{-2} . On the other hand, based on the J - V curve for the hole-only device in Fig. 5.2(c), the voltage drop of 0.12 V was derived at the same current density of 120 mA cm^{-2} per the cross-sectional area of the p -layer. This voltage drop is significantly low by taking the lateral gap of 0.05 mm between the two electrodes into account since the electric field between electrodes is calculated to only 24 V cm^{-1} ($0.12 \text{ V} / 0.005 \text{ cm}$). Very small required electric field strongly suggests that the lateral current flow through the p -layer is not a limiting factor of the photocurrent generation in the presently considered single-crystal cell.

The lateral hole-collection ability of the p -layer was further confirmed by increasing the length of the pn -homojunction (L) (Fig. 5.1). Irrespective of the irradiating light intensities (ranging from 0.05 sun to 10 sun), the photocurrent was

proportional to L , for L in the 0.2–1 mm range (Fig. 5.3(b)). Simultaneously, the photocurrent density per cross-sectional area of p -layer increases with the increase of L .²⁵⁾ Considering that the intensity of the electric field in the lateral direction can be regarded as nearly zero in the p -layer (Fig. 5.1) under a continuous metal electrode, we supposed that the holes in the p -layer are flowed by the diffusion process. Diffusion current allows to collect photo-generated holes independent of the lateral distance from $L = 0.2$ mm to the extremely far distance of $L = 1$ mm. Therefore, the p -layer can be regarded as a pseudo-electrode. Thus, we concluded that lateral hole transport and collection of holes from the entire area of the pn -homojunction occur, with the carrier collection efficiency (η_{CC}) of unity. As a result, the photocurrent density per area of the pn -homojunction can be calculated as shown in Fig. 5.3(a) (left vertical axis).

It should be noted that p -doped rubrene layer has another role for lateral hole extraction. When the intrinsic rubrene single crystal is directly attached to the pn junction without the p -layer (Fig. 5.1, blue rectangular part), an energy barrier at the intrinsic / p -type rubrene interface due to the different E_F value is formed. Since holes generated in a relatively upper lying HOMO level of the p -doped rubrene cannot come into the HOMO of intrinsic rubrene, the collection of photo-generated holes is prevented (Fig. 5.3(a), blue curve).

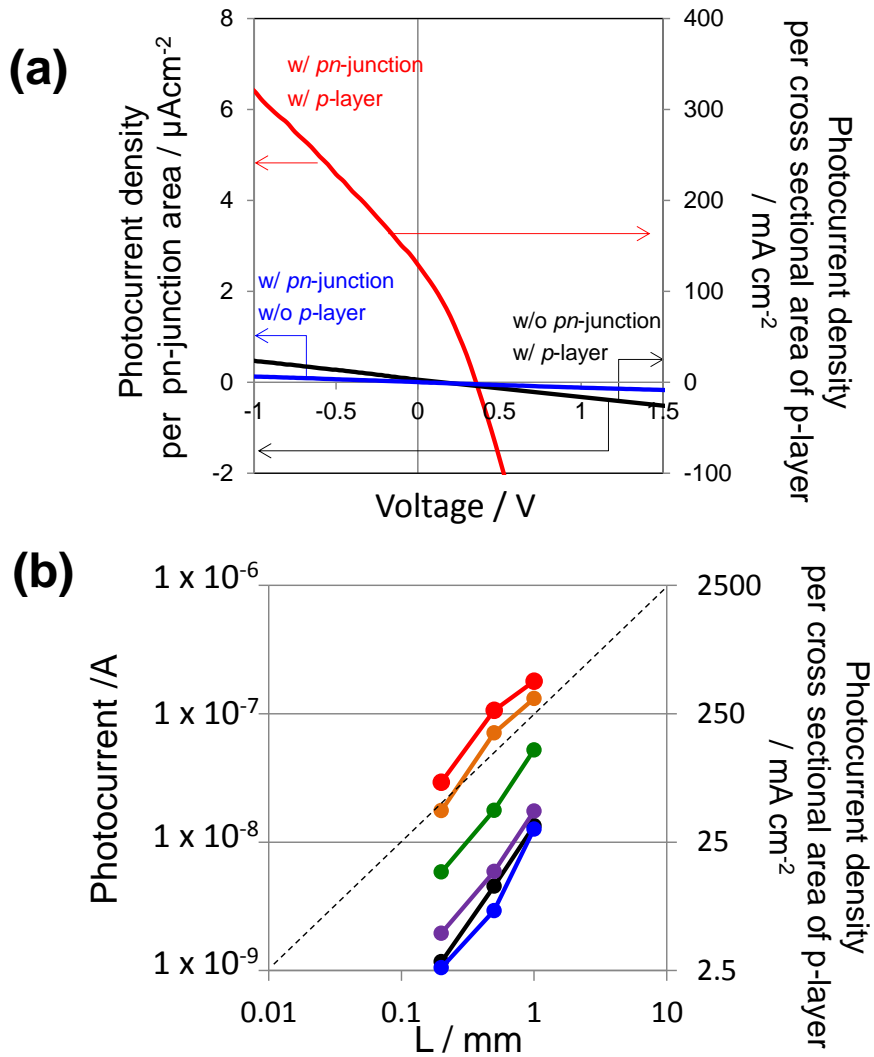


Fig. 5.3(a) J - V characteristics of doped organic single-crystal photovoltaic cells. Red curves: w/ p -layer, w/ pn -homojunction. The dashed red curve shows the dark current. Black curve: w/o pn -homojunction, w/ p -layer. Blue curve: w/ pn -homojunction, w/o p -layer. Simulated solar light at 10 suns was irradiated from the electrode side. (b) Dependence of the short-circuit photocurrent on the length of the pn -homojunction (L) (Fig. 1). Light intensities are 0.05 (blue), 0.1 (black), 0.5 (purple), 1 (green), 5 (orange), and 10 sun (red). The dotted line corresponds to the slope of unity.

5.3.3 Calculation for the exciton collection efficiency and exciton diffusion length

Fig. 5.4(a) shows the action spectra of the IQE of the short-circuit photocurrent, for the cell in Fig. 5.1, with the crystal thickness of 5.4 μm , irradiated by monochromatic light, from the substrate side (red curve) and from the electrode side (blue curve). The photocurrent action spectrum was observed even for the substrate side irradiation (red curve). The IQE value was about 4 times larger for the electrode side irradiation compared with the substrate side irradiation (Fig. 5.4(a), inset). Because the absorbance at the absorption peak wavelength (500 nm) is 3.1, the depth of the light penetration at which 90% of light is absorbed is 1.8 μm from the irradiation side of the rubrene crystal (Fig. 5.4(b), upper panel, red and blue curves). Therefore, in the case of substrate irradiation, to generate the photocurrent, the photogenerated excitons should travel $\sim 3.6 \mu\text{m}$ to reach the *pn*-homojunction. We quantitatively analyzed the exciton diffusion length. Fig. 5.4(b) shows the light absorption profiles for the substrate side (Fig. 5.4(b), upper panel, red curve) and electrode side (Fig. 5.4(b), upper panel, blue curve), for irradiation by 500-nm-wavelength monochromatic light. Diffusion profiles of excitons generated at the bottom surface of the crystal substrate (horizontal axis in Fig. 4(b), thickness = 0 μm) for various exciton diffusion lengths (σ) with the number of excitons decreasing to $(1/e)$ are shown in Fig. 5.4(b) (lower panel). The fraction of excitons that can diffuse to the *pn*-homojunction can be calculated by multiplying the fraction of absorbed photons (Fig. 5.4(b), upper panel) and the fraction of surviving excitons (Fig. 5.4(b), lower panel). The overall fraction of excitons that can diffuse to the *pn*-homojunction, i.e., the exciton collection efficiency (η_{EC}), can be calculated by summing up the fractions obtained for all starting points in the

light-absorbing profile. Fig. 5.4(c) shows the dependence of the calculated exciton collection efficiency (η_{EC}) on the exciton diffusion length (σ), for the substrate side (red dotted curve) and electrode side (blue dotted curve) irradiations. Because the distance between the light-absorbing profile and the *pn*-homojunction for the substrate irradiation (Fig. 5.4(b), upper panel, red curve) is significantly larger compared with that for the electrode irradiation (Fig. 5.4(b), upper panel, blue curve), η_{EC} increases rapidly with σ for the electrode side irradiation and somewhat slower for the substrate side irradiation. The ratio of η_{EC} for the substrate side irradiation ($\eta_{EC(sub)}$) to that for the electrode side irradiation ($\eta_{EC(elec)}$) is shown in Fig. 5.4(c) (black dotted curve).

As shown in Fig. 5.4(a), the IQE for the electrode side irradiation (IQE(elec)) is 2–4 times higher than that for the substrate side irradiation (IQE(sub)) (Fig. 5.4(a), inset). Here, the observed (IQE(elec)/IQE(sub)) is equal to ($\eta_{EC(elec)}/\eta_{EC(sub)}$) based on equation (1), because the exciton dissociation efficiency (η_{ED}) and carrier collection efficiency (η_{CC}) obviously do not depend on the light irradiation side. Therefore, by comparing (IQE(elec)/IQE(sub)) (Fig. 5.4(a), inset) and ($\eta_{EC(elec)}/\eta_{EC(sub)}$) (Fig. 5.4(c), black dotted curve), the exciton diffusion length (σ) was determined to be 2.7 μm for 500-nm-wavelength irradiation. The exciton diffusion length σ exhibited values ranging from 2.2 μm to 2.7 μm for wavelengths ranging from 420 nm to 500 nm (Fig. 5.4(d)). These values are in agreement with reported value (2–8 μm).¹⁴⁾

In the case of the electrode side irradiation by 500-nm-wavelength monochromatic light, the exciton collection efficiency (η_{EC}) reached 46% by assuming that half of the excitons diffuse to the opposite direction to the *pn*-homojunction, i.e., the substrate direction, and do not contribute to the photocurrent generation. On the other hand, carrier collection efficiency (η_{CC}) can be regarded to be unity. Based on

equation (1), exciton dissociation efficiency (η_{ED}) was estimated as 0.13%, using the IQE value of 0.06%.

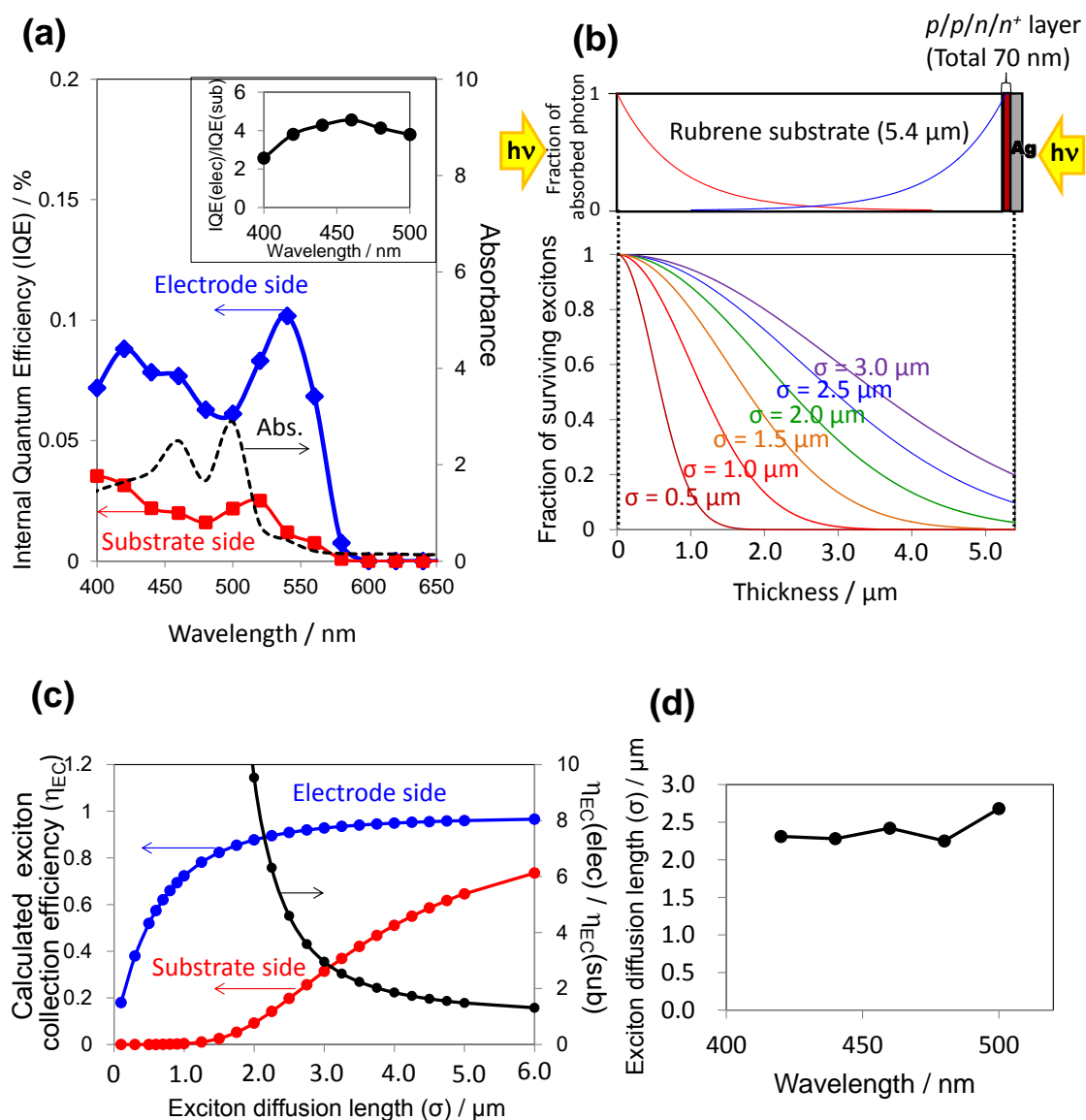


Fig. 5.4 (a) (upper) IQE action spectra of the short-circuit photocurrent for the cell in Fig. 5.1, with the crystal thickness of 5.4 μm , irradiated by monochromatic light from the substrate side (red curve) and from the electrode side (blue curve). The absorption spectrum of the 5.4- μm -thick rubrene single crystal (black broken curve) is also shown. (lower) Spectral dependence of $\text{IQE}(\text{elec})/\text{IQE}(\text{sub})$. (b) (upper) Light-absorption

profiles of the rubrene single crystal at the wavelength of 500 nm, irradiated from the substrate side (red curve) and from the electrode side (blue curve). (lower) Exciton diffusion profiles generated at the bottom surface of the crystal substrate, for various exciton diffusion lengths (σ) of 0.5, 1.0, 1.5, 2.0, 2.5, and 3.0 μm . (c) Dependence of the calculated exciton collection efficiency (η_{EC}) on the exciton diffusion length (σ) for the substrate side irradiation (red dotted curve) and electrode side irradiation (blue dotted curve). The ratio $\eta_{EC(sub)}/\eta_{EC(elec)}$ is also shown (black dotted curve). (d) Spectral dependence of the exciton diffusion length.

5.4. Conclusion

In conclusion, the operation of a doped organic single-crystal photovoltaic cell was demonstrated. Low exciton dissociation efficiency (η_{ED}) can be attributed to the relatively low electric field in the gradual depletion layer of finite width formed at the *pn*-homojunction mainly due to the very low doping concentration of 10 ppm. We think that η_{ED} would be increased by using donor/acceptor heterojunction accompanying the abrupt electrostatic potential gradient ²⁶⁾. The long exciton diffusion length in organic single crystals can eliminate the need for blended junctions. We posit that realizing whole doped organic single-crystal substrates is necessary for the further development of organic single-crystal photovoltaic cells.

5.5. References

- 1) R. J. Tseng, R. Chan, V. C. Tung, and Y. Yang, *Adv. Mater.* **20**, 435 (2008).
- 2) H. Mitsuta, T. Miyadera, N. Ohashi, Y. Zhou, T. Taima, T. Koganezawa, Y. Yoshida, M. Tamura, *Cryst. Growth Des.* **17**, 4622–4627 (2017).
- 3) Y. Nakayama, Y. Mizuno, T. Hosokai, T. Koganezawa, R. Tsuruta, A. Hinderhofer, A. Gerlach, K. Broch, V. Belova, H. Frank, M. Yamamoto, J. Niederhausen, H. Glowatzki, J.P. Rabe, N. Koch, H. Ishii, F. Schreiber, N. Ueno, *ACS Appl. Mater. Interfaces.* **8** 13499–13505 (2016).
- 4) R. M. Pinto, E. M. S. Maçôas, A. I. S. Neves, S. Raja, C. Baleizão, I. C. Santos, and H. Alves, **137**, 7104–7110 (2015).
- 5) M. Ichikawa, K. Nakamura, M. Inoue, H. Mishima, T. Haritani, R. Hibino, T. Koyama, and Y. Taniguchi, *Appl. Phys. Lett.*, **87**, 221113 (2005).
- 6) J. Takeya, M. Yamagishi, Y. Tominari, R. Hirahara, Y. Nakazawa, T. Nishikawa, T. Kawase, T. Shimoda, and S. Ogawa, *Appl. Phys. Lett.*, **90**, 1021120 (2007).
- 7) S. Haas, Y. Takahashi, K. Takimiya, and T. Hasegawa, *Appl. Phys. Lett.*, **95**, 022111 (2009).
- 8) H. Minemawari, T. Yamada, H. Matsui, J. Tsutsumi, S. Haas, R. Chiba, R. Kumai, and T. Hasegawa, *Nature*, **475**, 364 (2011).
- 9) R. W. I. de Boer, M. E. Gershenson, A. F. Morpurgo, and V. Podzorov, *Phys. Stat. Sol. A*, **201**, 1302 (2004).
- 10) M. Kikuchi, K. Takagi, H. Naito, and M. Hiramoto, *Org. Electron.*, **41**, 118–121 (2017).
- 11) P. Avakian and R. E. Merrield, *Phys. Rev. Lett.* **13**, 541 (1964).

- 12) V. Ern, P. Avakian, and R. E. Merrield, *Phys. Rev.* **148**, 862 (1966).
- 13) D. F. Williams and J. Adolph, *J. Chem. Phys.* **46**, 4252 (1967).
- 14) H. Najafov, B. Lee, Q. Zhou, L. C. Feldman, and V. Podzorov, *Nat. Mater.*, **9**, 938 (2010).
- 15) C. Ohashi, S. Izawa, Y. Shinmura, M. Kikuchi, S. Watase, M. Izaki, H. Naito, and M. Hiramoto, *Adv. Mater.*, **29**, 1605619 (2017).
- 16) R.A. Laudise, C. Kloc, P. G. Simpkins, and T. Siegrist, *J. Cryst. Growth.*, **187**, 449 (1998).
- 17) J. Takeya, K. Tsukagoshi, Y. Aoyagi, T. Takenobu, and Y. Iwasa, *Jpn. J. Appl. Phys.*, **44**, L1393 (2005)
- 18) X. Zeng, L. Wang, L. Duan, and Y. Qiu, *Crystal Growth & Design.*, **8**, 1617 (2008).
- 19) S. Tokito, K. Noda, and Y. Taga, *J. Phys. D: Appl. Phys.*, **29**, 2750 (1996).
- 20) T. Matsushima, Y. Kinoshita, and H. Murata, *Appl. Phys. Lett.*, **91**, 253504-1-3 (2007).
- 21) H. -H. Liao, L. -M. Chen, Z. Xu, G. Li, and Y. Yang, *Appl. Phys. Lett.*, **92**, 173303 (2008).
- 22) S. Hamwi, T. Riedl, and W. Kowalsky, *Appl. Phys. Lett.*, **99**, 053301-1-3 (2011).
- 23) N. Shintaku, S. Izawa, K. Takagi, H. Naito, and M. Hiramoto, *Org. Electron.*, **50**, 515–520 (2017).
- 24) The electron only device ($\text{Ag}/n^+/\text{n-type rubrene single crystal}/n^+/\text{Ag}$) also showed clear ohmic behavior similar to Fig. 2(c). Thus, we concluded that ohmic contacts to n -type rubrene single crystal are formed by using the n^+/Ag electrode.
- 25) The value of cross-sectional area of p -layer is calculated by 20 nm (the p -layer thickness) x 2 mm (pn -homojunction width). Since L increase causes the increase

of *pn*-homojunction area (L mm x 2 mm), magnitude of photocurrent generated by *pn*-homojunction increases with L . Thus, photocurrent density per cross-sectional area of *p*-layer increases with the increase of L .

- 26) Naoto Shintaku, Masahiro Hiramoto, Seiichiro Izawa, *J. Phys. Chem. C*, **122**, 5248–5253 (2018).

Chapter 6: Thesis Summary

The conclusions of this thesis and prospects for the future are presented in this chapter. The achievements of this study can be summarized as follows.

- 1) The operation of NTCDA single-crystal OPV cells using lateral electron transport with a macroscopic value of 30 μm was demonstrated.
- 2) The hole and electron ranges of C8-BTBT and PTCDI-C8 crystalline films of 0.4 and 0.2 mm were demonstrated, respectively.
- 3) A lateral organic superlattice junction, which completely collects both excitons and carriers, can be an alternative blended junction for OSCs.
- 4) The operation of a doped organic single-crystal photovoltaic cell was demonstrated. The large exciton diffusion lengths of organic single-crystals can eliminate the need for blended junctions. The *p*-doped single-crystalline layer can be regarded as a pseudo-electrode.

The results in this thesis can pave the way for the following future developments. First, a lateral device structure for OSCs could be achieved using a high-mobility organic single-crystal. Second, if whole-doped organic single-crystal substrates are realized, doped organic single-crystal wafers, similar to Si wafers, could be introduced.

List of publications

Papers of no.2-4 are included in this doctoral thesis.

- 1) “Doping Induced Photocurrent Enhancement in Organic Solar Cells Using High Photovoltage Organic Semiconductor”
Mitsuru Kikuchi, Yusuke Shinmura, Toshihiko Kaji, Takahiro Kono, Yuji Yoshida, and Masahiro Hiramoto
Jpn. J. Appl. Phys. **54**, 111601 (5 pages) (2015).
- 2) “Single Crystal Organic Photovoltaic Cells Using Lateral Electron Transport”
Mitsuru Kikuchi, Kenichiro Takagi, Hiroyoshi Naito, and Masahiro Hiramoto
Org. Electron., **41**, 118-121(2017).
- 3) “Doped Organic Single-Crystal Photovoltaic Cells”
Mitsuru Kikuchi, Sureerat Makmuang, Seiichiro Izawa, Kanet Wongravee, Masahiro Hiramoto
Org. Electron., **64**, 92-96 (2019).
- 4) “Lateral Alternating Donor/Acceptor Multilayered Junction for Organic Solar Cells”
Mitsuru Kikuchi, Masaki Hirota, Thidarat Kunawong, Yusuke Shinmura, Masahiro Abe, Yuichi Sadamitsu, Aye Myint Moh, Seiichiro Izawa, Masanobu Izaki, Hiroyoshi Naito, and Masahiro Hiramoto
ACS Applied Energy Materials, **2**, 2087–2093 (2019).

List of supplementary publications

- 1) “Hall Effect in Bulk-Doped Organic Single Crystals”
Chika Ohashi, Seiichiro Izawa, Yusuke Shinmura, **Mitsuru Kikuchi**, Seiji Watase,

Masanobu Izaki, Hiroyoshi Naito, and Masahiro Hiramoto

Adv. Mater., **29**, 1605619 (2017).

- 2) “Parts - per - Million - Level Doping Effects in Organic Semiconductor Films and Organic Single Crystals”

Masahiro Hiramoto, Mitsuru Kikuchi, and Seiichiro Izawa

Adv. Mater., **30**, 1801236 (2018).

Poster Presentations in International Conferences

- 1) “*pn*-Homojunction Organic Solar Cells Formed in the Co-deposited Films Using a Novel Push-Pull Type Organic Semiconductors”

Mitsuru Kikuchi, Yusuke Shinmura, Toshihiko Kaji, Takahiro Kono, Yuji Yoshida, and Masahiro Hiramoto

The 6th World Conference on Photovoltaic Energy Conversion (WCPEC-6), 6WePo.2.18, Kyoto International Conference Center, Kyoto, Japan, 2014/11/26.

- 2) “The Prototype of Lateral Electron-Collection-Type organic Solar Cells Using NTCDA Single Crystals”

Mitsuru Kikuchi, Kenichiro Takagi, Hiroyoshi Naito, and Masahiro Hiramoto

International Union of Materials Research Societies – International Conference on Electronic Materials 2016 (IUMRS-ICEM2016), J-D2-Poster-9, SUNTEC Singapore Convention & Exhibition Centre, Singapore, 2016/7/4-8.

- 3) “Single Crystal Organic Photovoltaic Cells Using Lateral Electron Transport”

Mitsuru Kikuchi, Kenichiro Takagi, Hiroyoshi Naito, and Masahiro Hiramoto

2017 E-MRS Spring Meeting, C5.18, Strasbourg Convention + Exhibition Centre, Strasbourg, France, 2017/5/23.

- 4) “Single Crystal Organic Photovoltaic Cells Using Lateral Electron Transport”

Mitsuru Kikuchi, Kenichiro Takagi, Hiroyoshi Naito, and Masahiro Hiramoto

The 27th Photovoltaic Science and Engineering Conference (PVSEC-27), 4ThPo.138, Lake Biwa Otsu Prince Hotel, Shiga, Japan, 2017/11/16.

Oral Presentations in Conferences (in Japanese)

- 1) “Junction Formation of Phase-Separated and Co-deposited C_{70} : H_2Pc Films”

Mitsuru Kikuchi, Masayuki Kubo, Toshihiko Kaji, Masahiro Hiramoto

The 74th The Japan Society of Applied Physics Autumn Meeting 2013, Doshisha University, 2013/9/18(18p-C6-2).

- 2) “Fabrication of npp^+ -Junction in DBP : C_{70} Co-deposited Films by Doping”

Mitsuru Kikuchi, Masayuki Kubo, Yuusuke Shinmura, Youhei Yamashina, Toshihiko Kaji, Masahiro Hiramoto

The 61st The Japan Society of Applied Physics Spring Meeting 2014, Aoyama Gakuin University, 2014/3/19 (19p-E9-4).

- 3) “The Prototype of Lateral Carrier Collection Type Organic Solar Cells Using a NTCDA Single Crystal”

Mitsuru Kikuchi, Kenichiro Takagi, Hiroyoshi Naito, and Masahiro Hiramoto

The 76th The Japan Society of Applied Physics Autumn Meeting 2015, Nagoya Congress Center, 2015/9/13 (15p-2N-7).

- 4) “Millimeter-Scale Hole Range in Single Crystalline Lateral Organic Photovoltaics”

Mitsuru Kikuchi, Yusuke Shinmura, Masaki Hirota, Masahiro Abe, Yuichi Sadamitsu, Aye Myint Moh, Masanobu Izaki, Hiroyoshi Naito, Masahiro Hiramoto

The 77th The Japan Society of Applied Physics Autumn Meeting 2016, TOKI MESSE Niigata Convention Center, 2016/9/15 (15a-A41-8).

- 5) “The D/A Superlattice Organic Solar Cells Using Lateral Carrier Transport in High Mobility Organic Single Crystalline Films”

Mitsuru Kikuchi, Aya Myint Moh, Masahiro Abe, Yuichi Sadamitsu, Hiroyoshi Naito, Masanobu Izaki, Masahiro Hiramoto

The 77th The Japan Society of Applied Physics Autumn Meeting 2016, Nagoya Congress Center, 2016/9/15 (15a-A41-9).

- 6) “Hall Effects for MoO₃-doped Homoepitaxial Rubrene Single Crystals”

Mitsuru Kikuchi, Chika Ohashi, Seiichiro Izawa, Masahiro Hiramoto

The 64th The Japan Society of Applied Physics Spring Meeting 2017, Pacific Yokohama, 2017/3/14 (14p-311-2).

- 7) “Hall Effects for Surface Doped Rubrene Single Crystals”

Mitsuru Kikuchi, Nitish Rai, Seiichiro Izawa, Masahiro Hiramoto

The 78th The Japan Society of Applied Physics Autumn Meeting 2017, Fukuoka Convention Center, 2017/9/5 (5a-A504-4).

- 8) “The D/A Superlattice Organic Solar Cells Using Lateral Carrier Transport in High Mobility Organic Single Crystalline Films”

Mitsuru Kikuchi, Aya Myint Moh, Masahiro Abe, Yuichi Sadamitsu, Hiroyoshi Naito, Masanobu Izaki, Masahiro Hiramoto

The 78th The Japan Society of Applied Physics Autumn Meeting 2017, Fukuoka Convention Center, 2017/9/5 (5a-A504-5).

- 9) “Doping Efficiency for Surface Doped Rubrene Single Crystals”

Mitsuru Kikuchi, Seiichiro Izawa, Masahiro Hiramoto

The 65th The Japan Society of Applied Physics Spring Meeting 2018, Waseda University, Nishiwaseda Campus, 2018/3/18 (18a-F104-2).

- 10) “Photovoltaic Cells Using Doped Rubrene Single Crystals”

Mitsuru Kikuchi, Sureerat Makmuang, Seiichiro Izawa, Masahiro Hiramoto

The 79th The Japan Society of Applied Physics Autumn Meeting 2018, Nagoya, 2018/9/21 (21p-432-7).

Poster Presentations in conferences (in Japanese)

- 1) “Doping Effect on the Cells Using a Novel Push-Pull Type Organic Semiconductor”

Mitsuru Kikuchi, Yusuke Shinmura, Toshihiko Kaji, Takahiro Kono, Yuji Yoshida, Masahiro Hiramoto

The 75th The Japan Society of Applied Physics Autumn Meeting 2014, Hokkaido University, 2014/9/17 (17a-PA2-14).

List of Patent (in Japanese)

- 1) 「高移動度有機半導体を用いた横方向キャリア収集型太陽電池」

“Lateral carrier collection type solar cells using high mobility organic semiconductors”

Yuichi Sadamitsu, Masahiro Abe, Hiroyoshi Naito, Masaki Hirota, Yusuke Shinmura, **Mitsuru Kikuchi**, Masahiro Hiramoto

Japanese patent application No. 2016-037354, 2016/2/29,

Acknowledgement

I greatly appreciate to Professor Masahiro Hiramoto at the Institute for Molecular Science, National Institute of Natural Science for a lot of meaningful discussions, advices, and teaching. I learned a lot of things from his enthusiastic attitude to study.

I express my sincere gratitude to Prof. Satoshi Kera, Prof. Hiroshi Yamamoto, Associate Prof. Toshiyasu Suzuki of IMS and Dr. Yuji Yoshida of AIST, for the review of this thesis.

I gratefully appreciate Dr. Yuji Yoshida and his group researchers at AIST, Prof. Masanobu Izaki and his group researchers at Toyohashi University of Technology, and Prof. Hiroyoshi Naito and his group researchers at Osaka Prefecture University for helpful discussions in the Core Research for Evolutional Science and Technology (CREST) project work and New Energy and Industrial Technology Development Organization (NEDO) project work.

I would like to thanks our group member; Assistant Prof. Toshihiko Kaji, Assistant Prof. Seiichiro Izawa, Dr. Masayuki Kubo, Dr. Yusuke Shinmura, Mr. Yohei Yamashina, Mr. Kenichi Abe, Dr. Chika Ohashi, Mr. Mikimasa Katayama, Dr. Naoto Shintaku, Mr. Masaki Hirota, Ms. Thidarat Kunawong, Ms. Sureerat Makmuang, Ms. Hidemi Sugihara and Ms. Megumi Kobayashi, for helpful discussion, a lot of advices, and encouragement.

I gratefully appreciate to WORLD INTEC CO., LTD. for a lot of supports.

Financial support from Core Research for Evolutional Science and Technology (CREST) of the Japan Science and Technology Agency (JST) and Advanced Research Program for Energy and Environmental Technologies of NEDO are gratefully

acknowledged.

Finally, I would like to express my sincere gratitude to everyone contributed to this my study.